Applied Physics Reviews

REVIEW ARTICLE | APRIL 24 2020

2D transition metal dichalcogenides, carbides, nitrides, and their applications in supercapacitors and electrocatalytic hydrogen evolution reaction

Shuoguo Yuan ; Sin-Yi Pang ; Jianhua Hao

Applied Physics Reviews 7, 021304 (2020)
https://doi.org/10.1063/5.0005141

Applied Physics Reviews REVIEW scitation.org/journal/are

2D transition metal dichalcogenides, carbides, nitrides, and their applications in supercapacitors and electrocatalytic hydrogen evolution reaction

Cite as: Appl. Phys. Rev. **7**, 021304 (2020); doi: 10.1063/5.0005141
Submitted: 18 February 2020 · Accepted: 27 March 2020 ·
Published Online: 24 April 2020

View Online Export Citation CrossMark

Shuoguo Yuan, Sin-Yi Pang, and Jianhua Hao[a)]

AFFILIATIONS

Department of Applied Physics, The Hong Kong Polytechnic University, Hong Kong, People's Republic of China

[a)]Author to whom correspondence should be addressed: jh.hao@polyu.edu.hk

ABSTRACT

The development of renewable energy conversion and storage devices, aiming at high efficiency, stable operation, environmental friendliness, and low-cost goals, provides a promising approach to resolve the global energy crisis. Recently, two-dimensional (2D) layered materials have drawn enormous attention due to their unique layered structure and intriguing electrical characteristics, which brings the unprecedented board applications in the fields ranging from electronic, optical, optoelectronic, thermal, magnetic, quantum devices to energy storage and catalysis. Graphene-based 2D layered materials show promising applications in energy storage and conversion owing to their high specific surface area, which have been used for supercapacitor electrode materials based on the electrical double-layer capacitance model. However, graphene has a limited value of theoretical electrical double-layer capacitance when the whole surface area is fully utilized. Among several classes of 2D layered materials beyond graphene, transition metal dichalcogenides, transition metal carbides, and nitrides may exhibit excellent electrochemical properties due to the distinctive features of these 2D materials, such as large specific surface area, good hydrophilic nature, highly exposed active edge sites, and ease of intercalation and modification. Therefore, careful design and construction of these 2D compounds make them become potential candidates used for electrochemical supercapacitors and electrocatalytic hydrogen evolution. This review emphasizes the recent important advances of the 2D layered materials composed of transition metal dichalcogenides, transition metal carbides, and nitrides for supercapacitors and electrocatalysts. Furthermore, we discuss the challenges and perspectives in this energy field in terms of the classes of two-dimensional layered materials.

TABLE OF CONTENTS

I. INTRODUCTION

In the past few decades, the consumption of non-renewable fossil fuels has raised great concerns about both the sustainability of global energy supply and environmental pollution. Therefore, designing and developing renewable energy conversion and storage devices are essential and beneficial to replace fossil fuels,[1–7] which promote the research on the high-performance supercapacitor and electrocatalytic hydrogen generation. Since the performances of energy storage and conversion devices highly depend on the properties of electrode materials, many studies have focused on the development of novel electrode materials with unique structural characteristics and functions to achieve high performance energy storage and conversion devices.[8–14]

Two-dimensional (2D) layered materials such as graphene have raised extensive interest for promising applications in energy storage and conversion owing to their high specific surface area.[1,15–18] For

example, graphene-based 2D materials have been used for supercapacitor electrode materials based on the electrical double-layer capacitance (EDLC) model, but graphene has a limited value of theoretical EDLC due to its high conductivity and specific surface area (~2630 m^2/g). The theoretical specific capacitance of monolayer graphene is approximately 21 $\mu F/cm^2$, and the corresponding specific capacitance is approximately 550 F/g when the whole surface area is fully utilized.[19] 2D porous polymers enjoy the merits of both polymers and 2D materials thanks to their high specific surface area, unique chemical structures, and abundant pores with active sites, which are beneficial for potential applications in supercapacitor and electrochemical catalysis.[20,21] However, preparing controllable 2D porous polymers still remains a challenge.

Recently, a large number of graphene analogs such as transition metal dichalcogenides (TMDs) and transition metal carbides and nitrides (MXenes) have been explored for the usage of electrodes due to their extraordinary physical and chemical properties.[22–31] The intriguing features of these 2D materials beyond graphene include a large specific surface area, good hydrophilic nature, highly exposed active edge sites, and ease of intercalation and modification, which make them become potential candidates in electrochemical supercapacitors and electrocatalytic hydrogen evolution. For example, MXenes are considered as very fascinating supercapacitor electrode materials, which are advantageous over other 2D materials such as graphene. The versatile functions of MXenes are attributed to their extremely metal conductivity, hydrophilic characteristics, and pseudocapacitance working mechanism. For instance, Ti_3CT_x materials possess a giant volumetric capacitance of 900 F/cm^3 (or 245 F/g) at a scan rate of 2 mV/s, which opens the unprecedented possibility of MXenes for supercapacitor applications. Currently, there is no specific review focusing on the field of supercapacitors and electrocatalytic hydrogen evolution based on the collection of the two classes containing TMDs and MXenes. In addition, recent progress of the two classes of 2D compounds is rapidly advancing, and the family members are significantly expanding. This review will concentrate on a brief overview of the latest research and development of TMDs and MXenes for supercapacitors and electrocatalytic hydrogen evolution reaction applications.

II. COMPOSITION AND STRCUTURE OF TMDs AND MXenes

The atomic composition and structure of the 2D material endow the differences in the physical and chemical properties. In the merit of semiconducting properties, the 2D material manifests its extensive uses in electronics such as memristors and field-effect transistors.[32,33] By virtue of the kinetics-favored architecture, ultrathin 2D materials have been widely studied and used in different fields since the first discovery of graphene.[34,35] Recently, the 2D materials are utilized in widespread applications for energy storage and conversion using a large surface-to-volume ratio in few- or mono-layered structures.[36] In particular, TMDs and MXenes, two rapidly emerging classes of layered 2D supercapacitor electrode materials, have been receiving broad interest in holding a large specific surface area, high mechanical stability, and good hydrophilic nature.[37–40] These layered materials not only have a strong chemical bonding to connect the in-plane atoms in each monolayer but also weak van der Waal (vdW) force to stack various layers, resulting in a form of bulk crystal.[41] Their crystal phases (Fig. 1) greatly affect material properties including the ion adsorption properties on the Helmholtz double layer in supercapacitors[42] and catalytic properties in water splitting,[43,44] rendering their uniqueness from the traditional bulk materials.

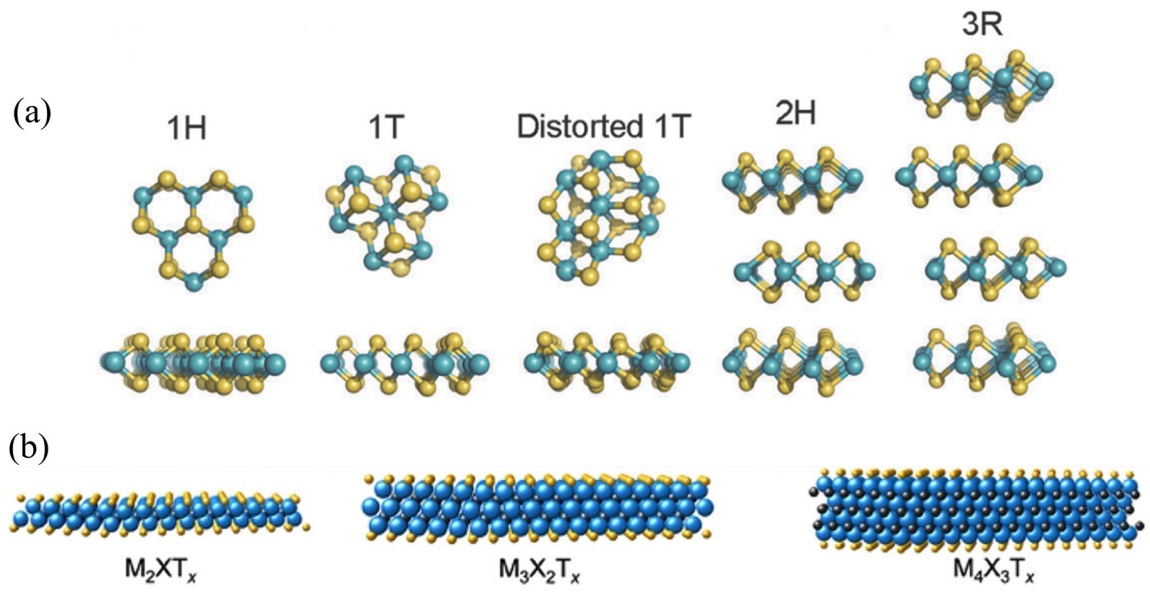

FIG. 1. (a) Crystal structures of MoS_2 with different polymorphisms including 1H, 1T, 1T′, 2H, and 3R structures.[43] Reproduced with permission from Voiry *et al.*, Chem. Soc. Rev. **44**, 2702–2712 (2015). Copyright 2015 Royal Society of Chemistry. (b) Crystal structures of MXenes in different layer arrangements by a chemical formula of $M_{n+1}X_n$, where n is 1, 2, or 3 (M_2X, M_3X_2, or M_4X_3), "M" represents the early transition metals (Ti, V, Cr, Nb, etc), and "X" is carbon and/or nitrogen.[39] Reproduced with permission from Gogotsi and Anasori, ACS Nano **13**, 8491–8494 (2019). Copyright 2019 American Chemical Society.

A. Transition metal dichalcogenides (TMDs)

TMDs are a chemically diverse class of layered compounds with a general formula of MX_2, where M represents a transition metal element (e.g., Mo and Te) and X is a chalcogen (e.g., S, Se, or Te).[46–49] The monolayer TMDs consist of a transition metal (TM) layer sandwiched by two chalcogen layers,[41] and they are in particular featured with the formation of different crystal polytypes [Fig. 1(a)],[43] which perform differently in catalysis and energy storage.[44,50] TMDs exist in different phases with crystal structures, including semiconducting 2H, metallic octahedral (1T), and distorted octahedral (1T′) phases. The numbers showing in different phases imply the stacking sequence of TMDs, for instance, 1H, 1T, 1T′, 2H, and 3R structures. In particular, the stacking sequence of 1H phase MX_2 is able to generate the 2H (AB sequence) or 3R (ABC sequence) phase.[43] The common semiconducting 2H phase MX_2 is the most thermodynamically stable one in nature. As a commonly used hydrogen evolution reaction (HER) catalyst, the Mo-edge of MoS_2 has been demonstrated to be active for HER, whereas the S-edge is inert for that.[51]

B. Transition metal carbides and nitride (MXenes)

MXenes as an emerging class of 2D materials were discovered by Gogotsi and Barsoum groups in 2011.[52] MXenes were produced by selective etching of the raw MAX phase materials, presented by a chemical formula of $M_{n+1}AX_n$, where n is 1, 2, or 3 (M_2AX, M_3AX_2, or M_4AX_3), "M" represents the early transition metals (Ti, V, Cr, Nb, etc), A stands for an element from groups 13 and 14, and "X" is carbon and/or nitrogen [Fig. 1(b)].[45] The MAX phases have a hexagonal structure with P63/mmc symmetry,[53] where the M layers are nearly hexagonally close-packed together and "X" atoms fill the octahedral sites.[54,55] Since M-A bonding (metallic bond) is weaker than that of M-X (mixed metallic-ionic covalent bond),[53,55–57] the "A" layer can be selectively etched from the MAX phase by HF[45] or NaOH[58] (Bayer process) and becomes an $M_{n+1}X_n$ (n = 1, 2, or 3) structure.

III. TMDs AND MXenes FOR SUPERCAPACITOR ELECTRODES

Supercapacitors have inspired great research interest in the past few decades, which possess high power density, very fast charge–discharge rate, and long cycle stability. According to their working principle, electrochemical capacitors as electrochemical energy storage devices depend on the contribution of double layer capacitance and/or pseudocapacitance.[59] Electric double layer supercapacitors are based on the theory of electric double layers. The capacitance results from the adsorption on the surface of the positive and negative materials to form a stable electric double layer to store energy. The supercapacitor is connected to the external circuit to supply the power when discharging. In addition, it is found that the formation of the electric double layer is actually a highly reversible physical process, and it does not involve chemical reactions. The electrodes used in the EDLC model are mainly traditional carbon-based and 2D materials, when considering these materials having a high specific surface area, a novel structure, and good electrical conductivity. Pseudocapacitive supercapacitors refer to EDLC supercapacitors with similar capacitive behavior. The difference between them is that the pseudocapacitive supercapacitors undergo a redox reaction. In addition, the redox reactions often involve changes in the polyvalent state, and thus, the stored energy is generally 10–100 times compared to an EDLC supercapacitor. However, the cycle performance of the material is poor due to the non-reversible redox process. The most widely used pseudocapacitive electrode materials include conducting polymers, transition metal oxides, and hydroxides.

In principle, whether a certain material is suitable for using supercapacitor electrodes or not really depends on its electrical conductivity, surface area, pore size distribution, surface modification, hybridization, doping, and hierarchical structure.[59–61] Moreover, other factors also play an important role in affecting the performance of supercapacitors, including the choice of electrode configuration, electrolytes, mass loading, and voltage applied. Currently, the development of supercapacitor technologies benefits from the novel 2D electrode materials. As one of the most promising candidates, TMDs and MXenes possess the enhanced electrochemical capability, long cycle life, and simple preparation process, which will facilitate various potential applications. Table I summaries various 2D materials and their synthesis methods, as well as the performances of supercapacitors.

A. TMDs

TMDs exhibit high performance electrochemical characterization derived from the large surface area, edge sites, and variable oxidation states, showing large energy storage capability in supercapacitors.[62,63] The typical 2H phase of MX_2 is most stable, but its electrochemical performance is often restricted by its poor electrical conductivity. For example, the semiconducting 2H phase MoS_2 exhibited a low specific capacitance of ∼100 F/g at a scan rate of 1 mV/s owing to its poor electrical conductivity.[64] Similar results have been reported in other compounds, such as WS_2[65] and $MoSe_2$.[66]

To overcome the barrier, Acerce *et al.* reported the metallic 1T-MoS_2 as an active electrode material for supercapacitors.[67] The high conductivity of 1T-MoS_2 ensures a fast electron transfer rate, which results in an enhanced supercapacitor performance. First, the metallic 1T-MoS_2 was prepared using the lithium intercalation with n-butyllithium, and the concentration of 1T-MoS_2 was as high as 70%. Then, the 1T-MoS_2 nanosheets were restacked into films via a vacuum filtration method, which can be used as a supercapacitor electrode [Fig. 2(a)]. As shown in Fig. 2(b), aqueous and organic electrolyte solutions were employed to estimate the electrochemical performance of the 1T-MoS_2 supercapacitor electrode. Obviously, the capacitance of the 1 T-MoS_2 electrode was much larger than that of the 2H-MoS_2 electrode. Noted that the highest volumetric capacitance of 650 F/cm^3 was achieved in the H_2SO_4 aqueous electrolyte at a scan rate of 20 mV/s [Fig. 2(c)]. In addition, all measured electrodes exhibited a capacitance retention over 90% after 5000 charge/discharge cycles at a current density of 2 A/g. Specifically, the 1T-MoS_2 electrode materials demonstrated excellent volumetric energy (0.11 Wh/cm^3) and power densities (1.1 W/cm^3), which exceeded many other reported electrode materials, as displayed in Fig. 2(d). The remarkable electrochemical properties of 1T-MoS_2 nanosheets could be attributed to the high conductivity, good hydrophilic nature, and restacking type. Therefore, an enhanced electrochemical performance of 2D TMD nanosheets can be achieved via the phase engineering from the semiconducting to the metallic phase.[61,68,69] Importantly, such a strategy could be extended to other 2D TMDs. Similarly, Khalil *et al.* reported stable metallic 1T-WS_2 nanoribbons via ammonia ion intercalation.[70] The specific capacitance of the 1T-WS_2 electrode materials showed a value of 2813 mF/cm^2, which was 12 times higher than that of semiconducting 2H-WS_2.

TABLE I. Various 2D materials of TMD and MXenes and their supercapacitor performances.

2D material category	Material	Synthesis method	Device type	Specific capacitance	Current density/ sweep rate	Cycling retention	References
TMDs	MoS_2	Chemical exfoliation	Supercapacitor electrode	∼650 F/cm^3	20 mV/s	5000/97%	67
	WS_2	Hydrothermal synthesis	Supercapacitor electrode	2813 mF/cm^2	0.5 A/m^2	2000/35%	70
	WTe_2	Liquid exfoliation	All-solid-state flexible supercapacitor	221 F/g	1 A/g	5500/91%	71
	VS_2	CVD growth	Supercapacitor electrode	860 F/g	5 mV/s	1000/85%	75
	$MoTe_2$	Chemical synthesis	Supercapacitor electrode	1393 F/g	5 mV/s	1000/98%	73
	TiS_2	Hot injection	Supercapacitor electrode	∼520 F/g	0.5A/g	…	74
	TaS_2	Liquid exfoliation	Supercapacitor electrode	508 F/cm^3	10 mV/s	4000/92%	72
	SnS_2	Solvothermal method	Supercapacitor electrode	431.82 F/g	1 A/g	2000/82%	89
	$MoSe_2/Bi_2Se_3$	Hot injection	Supercapacitor electrode	1451.8 F/g	1 A/g	3000/∼100%	83
	MoS_2–NiO	Solution-processed	Supercapacitor electrode	1080.6 F/g	1 A/g	9000/101.9%	63
	VS_2/MWCNTs	Ionic layer adsorption and reaction	All-solid-state flexible supercapacitor	860 F/g	5 mV/s	10 000/95.9%	81
	1T-MoS_2/Ti_3C_2 MXene	Hydrothermal	Symmetric supercapacitor	347 mF/cm^2	2 mA/cm^2	20 000/91.1%	133
MXenes	d-$Ti_3C_2T_x$	6M HF etching	Supercapacitor electrode	400 F/g	2 mV/s	10 000/90%	102
	d-$Ti_3C_2T_x$	12 M HF etching	Supercapacitor electrode	200 F/g	2 mV/s	10 000/90%	102
	MXene clay ($Ti_3C_2T_x$)	HCl + LiF	Supercapacitor electrode	900 F/cm^3	2 mV/s	10 000/∼100%	110
	NaOH–$Ti_3C_2T_x$	Alkaline-assist hydrothermal method	Supercapacitor electrode	314 F/g	2 mV/s	10 000/89.1%	58
	400-KOH–Ti_3C_2	HF etching and annealing	Symmetric supercapacitor	517 F/g	1A/g	5000/90.4%	119
	$Ti_3C_2T_x$	HCl + LiF	Supercapacitor electrode	380 F/g	10 mV/s	10 000/90%	117
	F-free Ti_3C_2	E-etching with intercalation	All-solid-state flexible supercapacitor	439 F/cm^3	10 mV/s	10 000/∼90%	118
	$Ti_3C_2T_x$	HCl + LiF	Supercapacitor electrode	435 F/g	2 mV/s	10 000/98%	120
	$Ti_3C_2T_x$	HCl + LiF	Asymmetric supercapacitor	118 F/g	1 A/g	3000/98.5%	121
	$Ti_3C_2T_x$	HCl + LiF	Flexible supercapacitor electrode	614.5 F/cm^3	5 mV/s	10 000/95%	122
	$Ti_3C_2T_x$	HF etching	Supercapacitor electrode	239 mF/cm^2	10 mV/s	10 000/100%	123
	$Ti_3C_2T_x$ MXene/CNF	HCl + LiF	Micro-supercapacitor	298 F/g	2 mV/s	10 000/100%	124
	p-C_3N_4@ Ti_2CT_x	HF etching and annealing	Supercapacitor electrode	327 F/g	10 mV/s	5000/96.2%	125
	N, O co-doped C@ Ti_3C_2	HF etching	Symmetric supercapacitor	250.6 F/g	1 A/g	5000/94%	126
	RuO_2@ MXene	HCl + LiF	Micro-supercapacitor	864.2 F/cm^3	1 mV/s	10 000/90%	127
	MXene/CNT-hydroquinone	HCl + LiF	All-solid-state flexible supercapacitor	1080 F/g	2 mV/s	5000/90%	128
	MXene/MPFs	HCl + LiF	All-solid-state flexible supercapacitor	326.1 F/g	0.1 A/g	7000/95.9%	129
	AC/$Ti_3C_2T_x$	HCl + LiF	Supercapacitor electrode	126 F/g	0.1 A/g	10 000/57.9%	130
	MXene/RGO	HCl + LiF	Flexible supercapacitor	90 F/cm^3	1 A/g	10 000/85%	134
	SA-MXene	HCl + LiF	Micro-supercapacitor	720.7 F/cm^3	1 A/g	4000/94.7%	135

TABLE I. (*Continued*.)

2D material category	Material	Synthesis method	Device type	Specific capacitance	Current density/ sweep rate	Cycling retention	References
	3D PANI@M- $Ti_3C_2T_x$	HCl + LiF	Asymmetric supercapacitor	827 F/cm^3	5 V/s	20 000/85.7%	136
Layered double hydroxide (LDH)	(Ni,Co)Se_2/ NiCo-LDH	Hydrothermal	Asymmetric supercapacitor	1224 F/g	2 A/g	3000/~90%	137
Graphene	$Mn_{0.1}Ni_{0.9}MoO_4$/rGO	Hydrothermal	All-solid-state supercapacitor	688.9 F/g	0.5 A/g	200/96.1%	138
Boron nitride/ graphene	h-BN/rGO	Hydrothermal	Asymmetric supercapacitor electrode	824 F/g	4 A/g	4000/89%	139

The enhanced capacitance value was attributed to the greatly improved electrical conductivity of the 1T-WS_2 electrode. In addition, the electrode also exhibited a good stability even under high current scans, resulting from the stable ammonia-ion interaction.

Compared with semiconducting S-based and Se-based TMDs, which are required to transform via phase engineering, the stable metallic phase of Te-based WTe_2 shows much better electrical conductivities at room temperature, which is beneficial to improving the supercapacitor performance. Yu *et al.* reported that the metallic $1T_d$-WTe_2 nanosheets were prepared by liquid exfoliation.[71] These $1T_d$-WTe_2 nanosheets were assembled into stable films, and therefore, all-solid-state flexible supercapacitors were fabricated. The fabricated supercapacitors exhibited a mass capacitance of 221 F/g [Fig. 3(a)] and a stack capacitance of 74 F/cm^3. In addition, the devices could power light-emitting diodes (LEDs) for 40 s after being charged to 3 V in 10 s. Furthermore, they showed an excellent volumetric energy of 0.01 Wh/cm^3 and a power density of 83.6 W/cm^3, respectively [Fig. 3(b)]. Wu *et al.* reported that very large-sized conductive monolayer sub-nanopore TaS_2 was prepared by acid-assisted exfoliation.[72] The as-produced metallic TaS_2-based micro-supercapacitor exhibited a large volumetric capacitance of 508 F/cm^3 at a scan rate of 10 mV/s and a high energy density of 58.5 Wh/L [Fig. 3(c)]. Moreover, other metallic phases of TMDs were also used as potential supercapacitor electrode materials, such as $MoTe_2$,[73] $MoSe_2$,[74] VS_2,[75,76] TiS_2,[77] and VSe_2.[78]

The combination of 2D TMDs with highly conductive materials has been demonstrated to be a reasonable approach to enhance the supercapacitor performance due to the strong synergetic effect of individual materials,[79–81] including conducting polymers, graphene, microporous carbon, and 2D compounds. In particular, conducting polymers are promising additives, which significantly enhance the capacitive performance of 2D TMDs because of their high redox-active capacitance, moderately high electrical conductivity, low cost, and high intrinsic flexibility. Combining polyaniline (PANI) nanoneedle arrays with MoS_2 nanosheets were reported using an ice-reaction process.[82] This highly electrochemically active 2D MoS_2@PANI composite with a large surface area and good electrical conductivity exhibited a high specific capacitance of 853 F/g at a current density of 1 A/g. Meanwhile, a very high energy density of 106 Wh/kg at a power density of 106 kW/kg was also achieved, which was significantly higher than those reported for MoS_2-based materials and commercial supercapacitor devices. Yang *et al.* reported that the $MoSe_2/Bi_2Se_3$ hybrids demonstrated superior capacitive performances of 1451.8 F/g at 1 A/g and 750 F/g at 20 A/g, respectively,[83] which were higher than two times of that of pure $MoSe_2$ and three times of that of pure Bi_2Se_3 at identical current densities [Fig. 3(d)]. In addition, any obvious changes were not found in the $MoSe_2/Bi_2Se_3$ hybrids after 3000 charge–discharge cycles at 10 A/g, indicating an excellent cycling stability ascribed to the faster transport rates of electrons and ions, smaller resistance, and more stable kinetic reversibility between Bi_2Se_3 and $MoSe_2$.

It is worthy of remark that various structures derived from TMDs have been used as supercapacitor electrodes, which exhibit enhanced performance.[84–87] Peng *et al.* reported that varied hierarchical structures with solid, yolk-shell, double-shell, and hollow spheres assembled from CoS_2 nanosheets have been synthesized using a simple hydrothermal method.[88] It is noted that the CoS_2 hollow sphere based

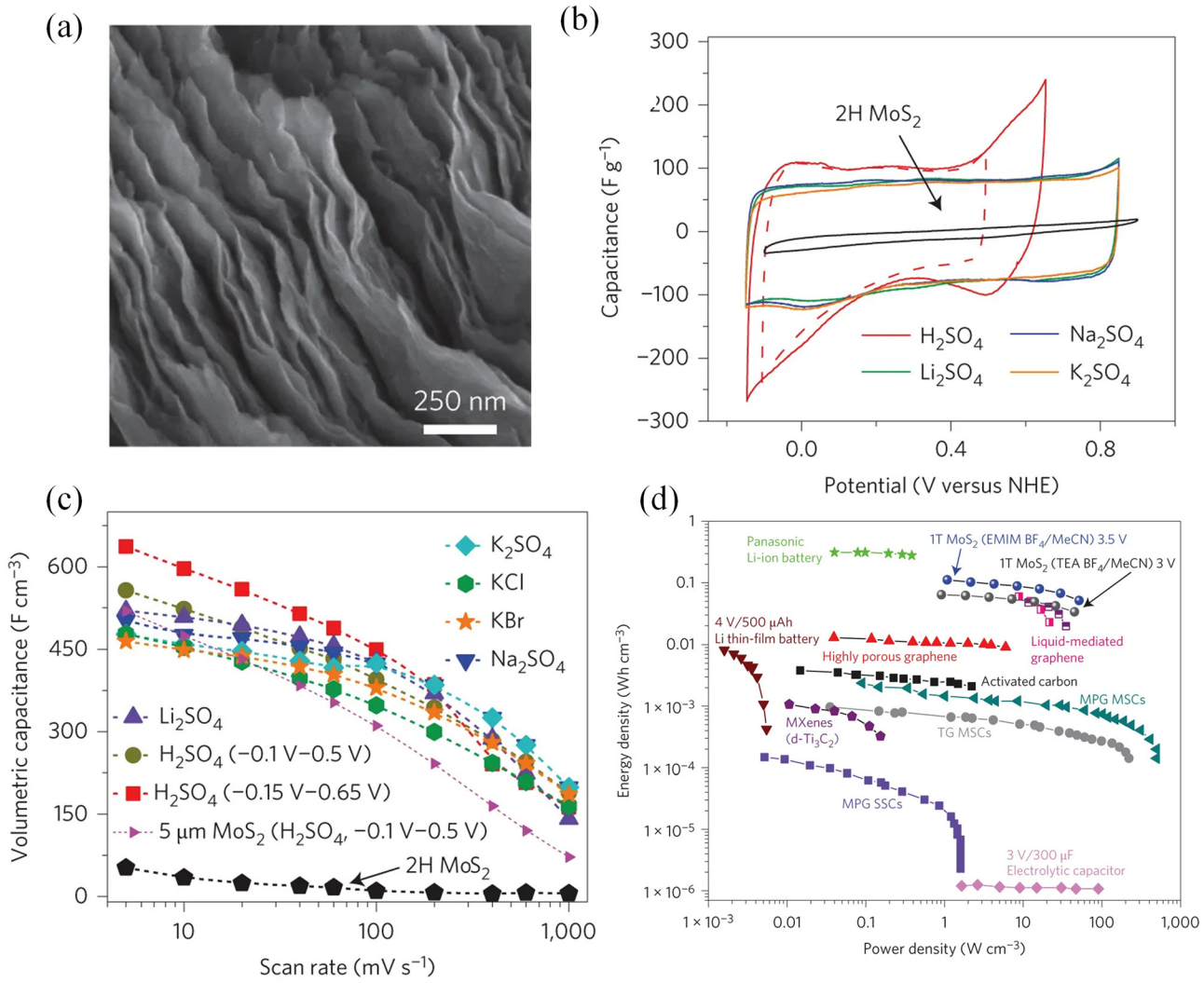

FIG. 2. The electrochemical performance of 1T-MoS_2 as supercapacitor electrodes: (a) side view of restacking MoS_2 nanosheets. (b) Cyclic voltammetry (CV) profiles of 2H and 1T-MoS_2 in different electrolyte solutions. (c) The volumetric capacitance of the 1T-MoS_2 with scan rates for different electrolytes. (d) Ragone plot of the volumetric power and energy densities for 1T-MoS_2 and other reported electrode materials.[67] Reproduced with permission from Acerce *et al.*, Nat. Nanotechnol. **10**, 313–318 (2015). Copyright 2015 Springer Nature Publishing.

electrode showed the highest specific capacitance of 1301 F/g at a current density of 1 A/g, as shown in Fig. 3(e). In addition, a specific capacitance of 450 F/g still remained on the electrode based on CoS_2 hollow spheres even at a high current density of 20 A/g, indicating the good rate capability. The excellent supercapacitor performance of CoS_2 hollow spheres can be attributed to the specific 3D architecture with a high surface area for the faradic redox reaction and suitable mesopore distribution for the mass transfer of electrolytes. The morphology of TMD materials has a significant effect on the electrochemical performance. Parveen *et al.* showed that the flower-like SnS_2 exhibited better capacitive performance than the sheet-like SnS_2 and ellipsoid-like SnS_2.[89] The flower-like SnS_2 electrodes showed a high specific capacitance of ~431.82 F/g at a current density of 1 A/g. The outstanding electrochemical performance of the flower-like SnS_2 materials could be ascribed to the larger specific surface area and better average pore size. In addition, the SnS_2 nanostructures (flower-like, sheet-like, and ellipsoid-like) also displayed good cycling stability, as shown in Fig. 3(f).

Interestingly, 2D TMD based materials possess good mechanical strength with flexibility characteristics, which have been demonstrated as promising flexible supercapacitors.[7,67] The flexible supercapacitors are able to meet the power requirements of compact applications, such as wearable devices. The flexible films composed of 2D TMD nanosheets can be easily fabricated through a vacuum filtration method. The vdW interaction between 2D TMD nanosheets ensured the mechanical stability of the fabricated films and enabled the direct use of the films as electrodes without additional polymer binders. Wang *et al.* presented that a flexible in-plane solid-state supercapacitor can

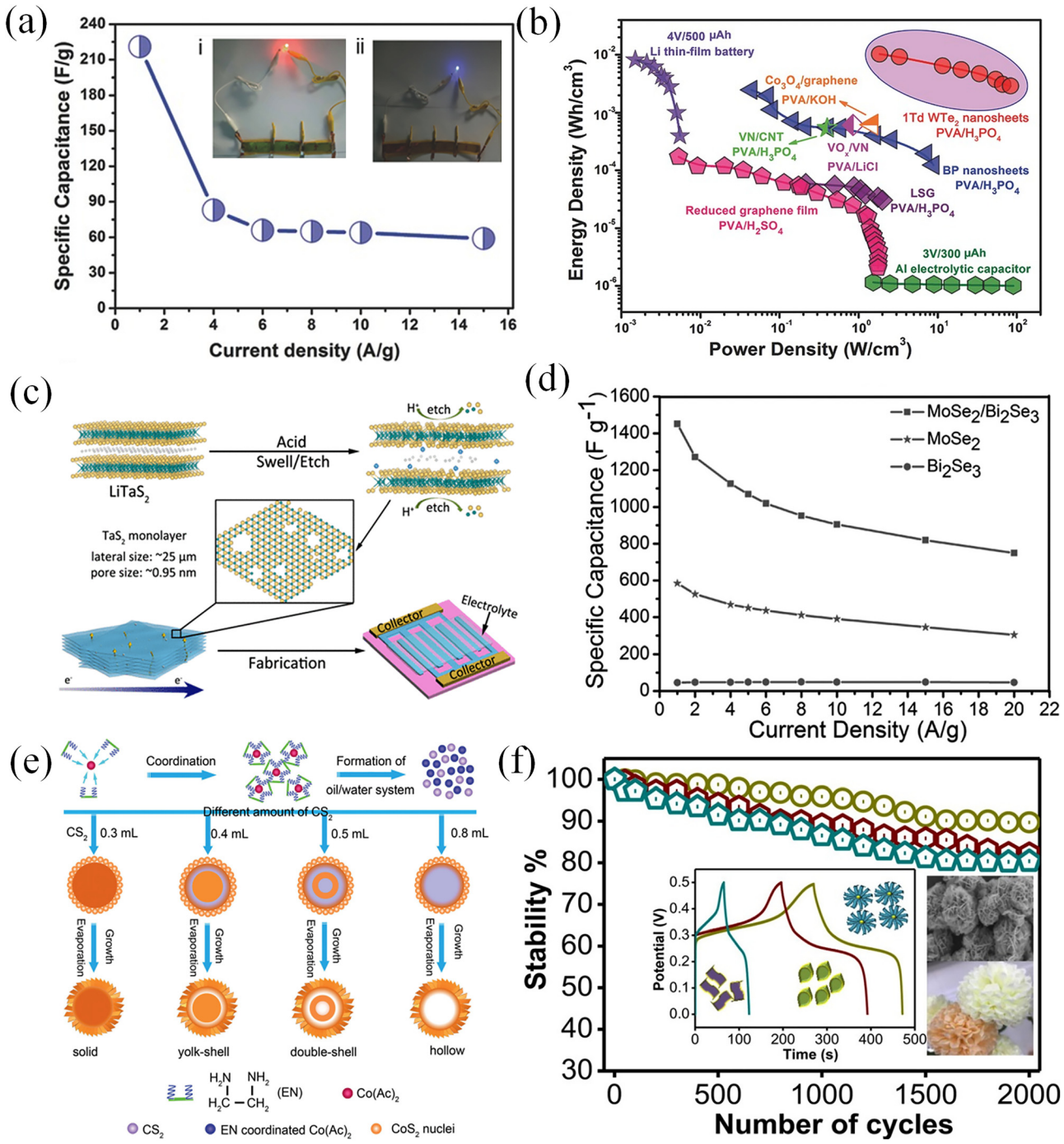

FIG. 3. (a) Specific capacitance of 1.1 μm WTe_2 as a function of current density. (b) The comparison of volumetric energy and power densities of $1T_d$-WTe_2 and other reported materials.[71] Reproduced with permission from Yu *et al.*, Adv. Mater. **29**, 1701909 (2017). Copyright 2017 Wiley-VCH. (c) Metallic sub-nanopore monolayer TaS_2 was produced via acid-assisted exfoliation and then a micro-supercapacitor was fabricated.[72] Reproduced with permission from Wu *et al.*, J. Am. Chem. Soc. **140**, 493–498 (2018). Copyright 2018 American Chemical Society. (d) Specific capacitance as a function of current density with the $MoSe_2/Bi_2Se_3$ hybrids, pure $MoSe_2$, and Bi_2Se_3.[83] Reproduced with permission from Yang *et al.*, Adv. Funct. Mater. **27**, 1703864 (2017). Copyright 2017 Wiley-VCH. (e) Schematic diagram of synthesis for the solid, yolk-shell, double-shell, hollow spheres, and bulk CoS_2, respectively.[88] Reproduced with permission from Peng *et al.*, Adv. Funct. Mater. **24**, 2155–2162 (2014). Copyright 2014 Wiley-VCH. (f) Capacitance retention of the EL-SnS_2, FL-SnS_2, and SL-SnS_2 electrodes; the inset shows their profiles at a current load of 1 A/g.[89] Reproduced with permission from Parveen *et al.*, ACS Omega **3**, 1581–1588 (2018). Copyright 2018 American Chemical Society.

be made by using metallic few-layer VSe_2 nanosheets. The prepared supercapacitor has a high power density, which is comparable to that of graphene-based supercapacitors. After being charged to 2.2 V for 15 s, the supercapacitors could power up red, yellow, and green LED lights with the lowest working voltage from 1.6 V to 1.8 V. More importantly, the flexible supercapacitor showed robust stability even after 10 000 bending cycles [Figs. 4(a) and 4(b)].[77] The flexible solid-state symmetric supercapacitor device prepared from VS_2/multiwalled carbon nanotubes (MWCNTs) exhibited maximum gain in a specific capacitance value of 182 F/g at a scan rate of 2 mV/s along with a specific energy of 42 Wh/kg and a superb stability of 93.2% over 5000 cycles, as shown in Fig. 4(c).[81] Figure 4(d) displays a flexible 1T-MoS_2 film deposited on a polyimide substrate using a simple filtration technique.[67]

B. MXenes

Electrochemical capacitors refer to an electrochemical energy storage technology based on the double layer capacitance and/or pseudocapacitance.[92] MXenes are regarded as promising materials because their sheet-like structure renders them a large surface area, contributing to more capacitance than traditional layered materials such as graphene or phosphorene.[93–96] Different synthesis methods affected the chemical and physical properties of MXenes.[97,98] Hydrofluoric acid (HF) etching is a common approach to achieve selective etching of "A" layers from the MAX phases. The mechanism is based on the difference in bond strength, where the M-A bond is generally weaker than the M-X bond.[53,56,57,99] In the inherently nanolayered MAX phase materials, the "A" layers were etched by the HF acid to form a fluoride with the release of hydrogen gas

$$M_{n+1}AX_n + 3HF \rightarrow AF_3 + 3/2H_2 + M_{n+1}X_n. \quad (1)$$

The -F and -OH termination groups could be found on the surface of the MXenes during the HF etching process, as described in the following equations:

$$M_{n+1}X_n + 2HF \rightarrow M_{n+1}X_nF_2 + H_2, \quad (2)$$

$$M_{n+1}X_n + 2H_2O \rightarrow M_{n+1}X_n(OH)_2 + H_2. \quad (3)$$

In general, the MAX phase powder was immersed in 10% or 50% concentrated HF with stirring at room temperature to complete the etching [Fig. 5(a)].[91] The etching time depended on types of materials; for

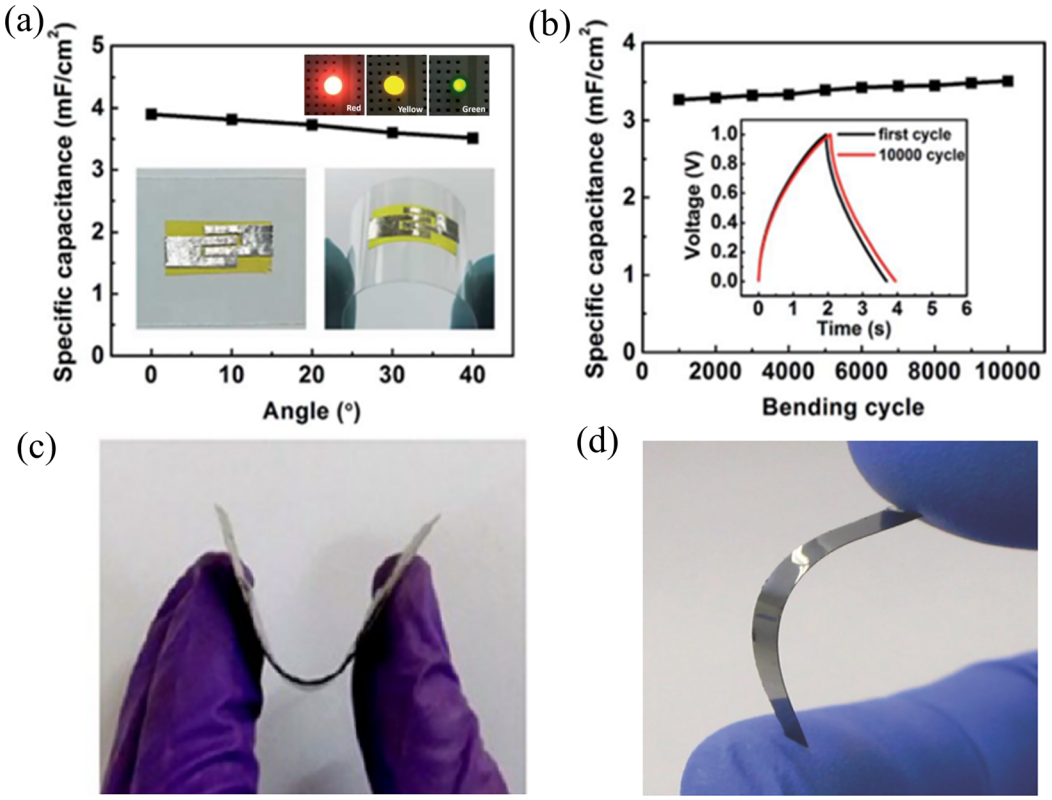

FIG. 4. (a) The specific capacitance as a function of the bending degree. The left and right insets show the flat and curved states of the supercapacitor. Demonstration of red, yellow, and green LED lights powered by in-plane supercapacitors. Reproduced with permission from (b). The stability of the specific capacitance of the VSe_2 supercapacitor; the inset displays the charge–discharge curves of the supercapacitor at a scan rate of 2 mA/cm^2 after 10 000 bending cycles.[77] Reproduced with permission from Wang *et al.*, J. Mater. Chem. A **6**, 8299–8306 (2018). Copyright 2018 Royal Society of Chemistry. (c) Photograph of the flexible solid-state symmetric supercapacitor device based on the VS_2/MWCNT electrode.[81] Reproduced with permission from Pandit *et al.*, ACS Appl. Mater. Interfaces **9**, 44880–44891 (2017). Copyright 2017 American Chemical Society. (d) Photograph of a flexible 1T-MoS_2 film deposited on a polyimide substrate.[67] Reproduced with permission from Acerce *et al.*, Nat. Nanotechnol. **10**, 313–318 (2015). Copyright 2015 Springer Nature Publishing.

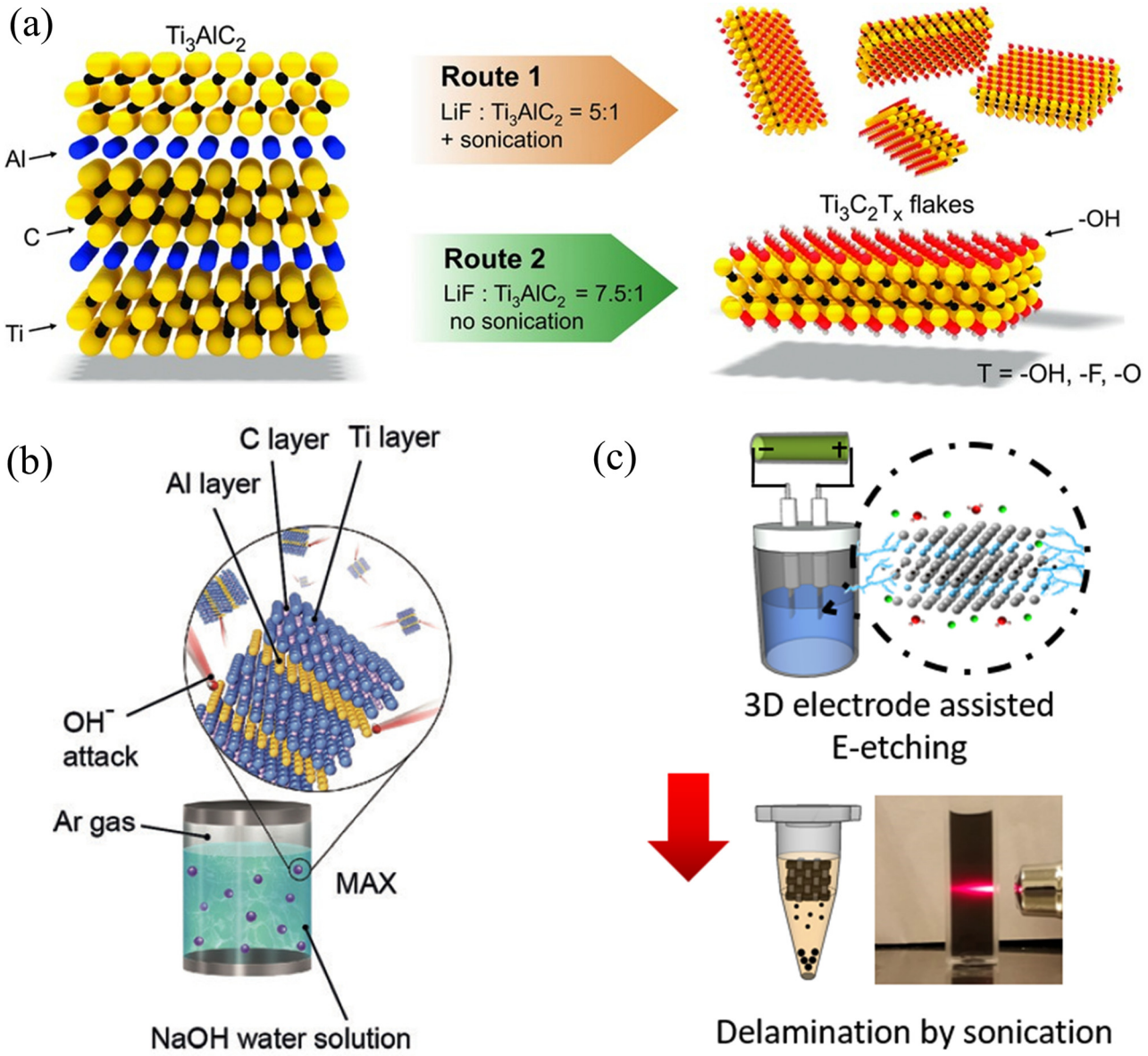

FIG. 5. Schematics for synthesizing MXene. Three synthesis methods are presented: (a) indirect HF etching. In the presented method, the mixture of LiF powder and HCl solution was utilized to produce the *in situ* formation of the HF acid on the surface of the MXene.[91] Reproduced with permission from Lipatov *et al.*, Adv. Electron. Mater. **2**, 1600255 (2016). Copyright 2016 Wiley-VCH. (b) Alkali treatment. In the second method, high temperature and high pressure were used to assist the formation reaction of the Al–OH bonding by alkali solution. As a result, the aluminum layer was selectively removed from the MAX phase material.[58] Reproduced with permission from Li *et al.*, Angew. Chem., Int. Ed. **130**, 6223–6227 (2018). Copyright 2018 Wiley-VCH. (c) Electrochemical etching (E-etching) method. The electrochemical etching mechanism based on the reaction priority of M-X bonding and A-X bonding. The A-X bonding is first decomposed by the electrochemical reaction to complete selective etching. A further reaction may drive the reaction to complete etching of all metal layers but not selective etching.[90] Reproduced with permission from Pang *et al.*, J. Am. Chem. Soc. **141**, 9610–9616 (2019). Copyright 2019 American Chemical Society.

example, vanadium (V)- and molybdenum (Mo)-based MAX phase materials usually required more than 3 days to achieve the selective etching.[100,101] For MXenes, the termination groups and the concentration of the etchant play important roles in their electrochemical properties. Hu *et al.* disclosed a special electrochemical behavior of $Ti_3C_2T_x$ MXene, by adjusting the concentration of the etchant to control over the interlayer water and functional groups.[102] Surprisingly, the MXenes etched from 6 M HF had a higher supercapacitance than that etched from 12 M HF, even though the gravimetric surface area of the 12 M HF etched $Ti_3C_2T_x$ sample (40.5 m^2/g) was one order magnitude higher than that of the 6 M HF etched $Ti_3C_2T_x$ sample (3.5 m^2/g). The results revealed that the surface functional group and the interlayer

water are more dominant factors on the electrochemical cap of MXenes compared to the specific surface area. The sample etched from 6 M HF exhibited a larger interspace, so the higher accessibility of water molecules between the active sites of the MXene led to their high capacitance of 400 F/g at a scan rate of 2 mV/s.

Instead of directly using HF acid to attain MXenes from their MAX phases, an alternative etching method was developed as an *in situ* formation of HF. The HF can be formed by mixing the strong acid and F salt to remove the "A" layers from the MAX phases selectively. This method can terminate the surface of MXenes with -Cl groups and provide the products with a better Li-ion-battery storage property by the enlarged interlayer spacing.[103] Cations dissociated from the fluoride salt cause an intercalation of the cations and water content to the MXenes, weakening the interaction between MXene interlayers. By using the indirect HF etching, the etched MXene can directly process to delamination without an extra step of intercalation.[45,104] For most of the applications of the MXenes, delamination is a necessary step for the MXenes to achieve a better performance. Liquid exfoliation and intercalation delamination were mostly used for MXene production.[105,106] Polar organic molecules such as dimethyl sulfoxide (DMSO), thiourea, and urea were used as intercalants.[107,108] The intercalated MXene, subject to mechanical vibration or sonication in water, produced freestanding MXene "papers" or "flakes."[98,109] Ghidiu *et al.* demonstrated an innovative approach to fabricate an 2D electrode for a high-performance supercapacitor.[110] $Ti_3C_2T_x$ was prepared by dissolving 1.98 g LiF in 6 M HCl. Figure 6 shows that the rolled pseudocapacitive Ti_3CT_x films exhibit a high volumetric capacitance of 900 F/cm^3 (or 245 F/g) at a scan rate of 2 mV/s, which opens the possibility of MXene as a promising supercapacitor.

Fluorine containing solution provides a method for MXene mass production. However, the presence of highly toxic HF hampers further development of the MXenes. Li *et al.* reported an alkali-etching strategy to produce $Ti_3C_2T_x$ from MAX phase Ti_3Al_2C [Fig. 5(b)].[58] Using neither a halide reactant nor high temperature, concentrated NaOH solution was used for the etching process at a mild temperature. Alkali can possibly remove the outer layer Al of the MAX phases due to the strong binding ability of OH with amphoteric element Al;[111] however, there are a few literature studies reported on the selective etching of Al

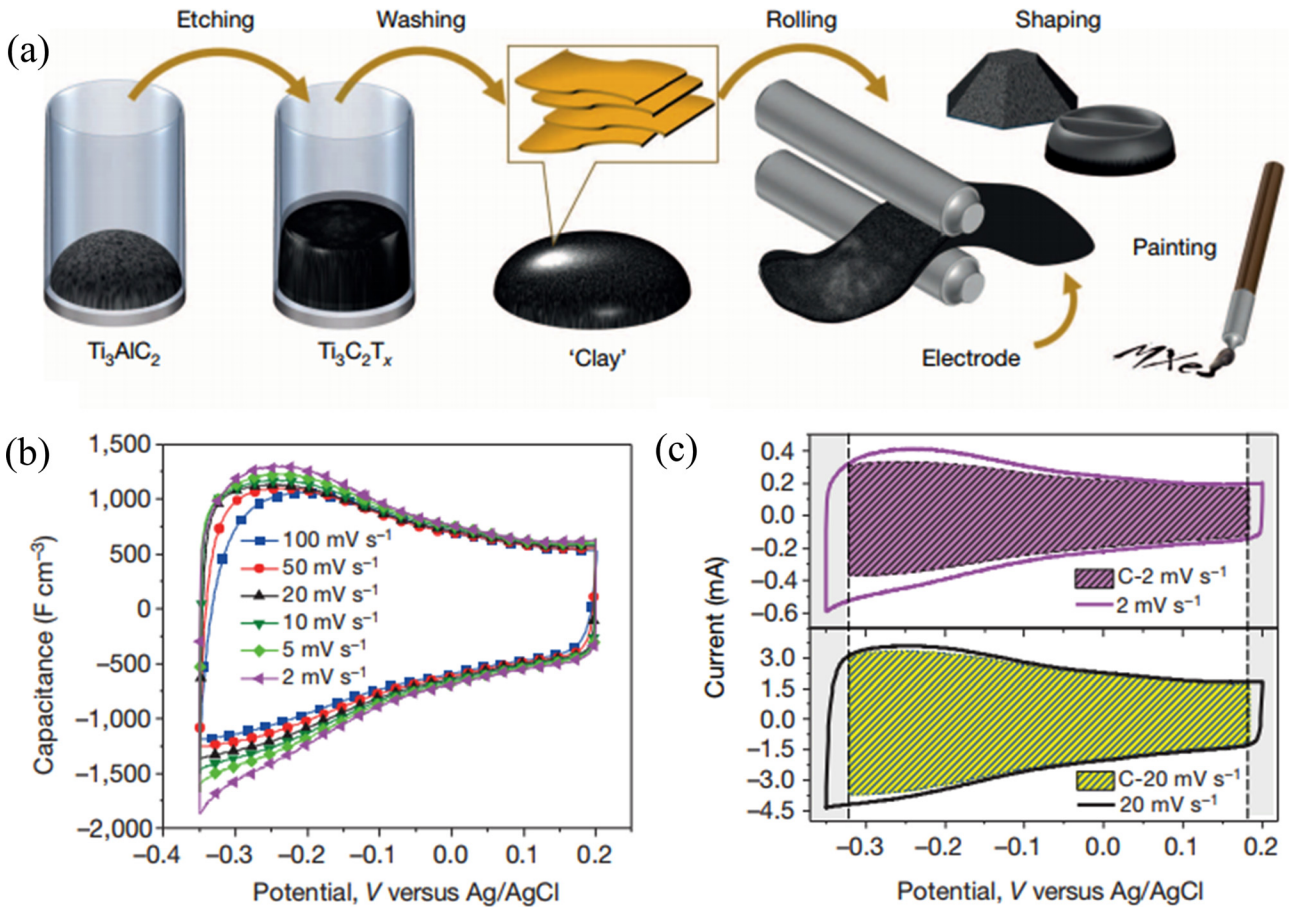

FIG. 6. (a) Schematic of MXene clay synthesis and electrode preparation. Electrochemical performance of rolled and free-standing electrodes. (b) CVs at different sweep rates for a 5-mm-thick electrode in 1M H_2SO_4. (c) CVs collected at 2 mV/s and 20 mV/s with their deconvolution, which illustrate their capacitive ('C-') contributions, whereas the vertical line depicts the calculation limitation in the deconvolution process.[110] Reproduced with permission from Ghidiu *et al.*, Nature **516**, 78–81 (2014). Copyright 2014 Springer Nature Publishing.

by alkaline etchants.[112,113] It should be noted that this method still has a challenge in producing accordion-like MXenes due to the formation of Na/K–Ti–O composites.[114,115] The thermo-assisted reaction can solve the kinetic problem caused by the presence of O/OH protective layers on the Ti_3Al_2C surface. The -F functional group free MXene exhibit a favorable performance toward the electrochemical capacitance storage due to their -O rich surface. The etching mechanism of fluorine-free synthesis of high-purity MXene via alkali treatment is depicted as the following equations:

$$Ti_3AlC_2 + OH^- + 5H_2O \rightarrow Ti_3C_2(OH)_2 + Al(OH)_4^- + 5/2H_2, \quad (4)$$

$$Ti_3AlC_2 + OH^- + 5H_2O \rightarrow Ti_3C_2O_2 + Al(OH)_4^- + 7/2H_2. \quad (5)$$

Since this alkaline-based etching involved none of F-containing etchants, a fluoride-free but -O or -OH functional group rich $Ti_3C_2T_x$ MXenes ($NaOH–Ti_3C_2T_x$) could be fabricated, presenting better electrochemical capacitance than that of the HF etched MXene. It is proposed that the -O/-OH termination groups of MXenes are beneficial to redox-related capacitance where the -F functional group is less favorable for redox processes.[42,116] The MXenes exhibited a promising capacitance of 314 F/g at a scan rate of 2 mV/s, as shown in Fig. 7. The F-free MXenes open a new possibility to energy storage materials; however, their lack of fast charge/mass transport dynamics is one of the major barriers to practical use. Moreover, this alkaline-based etching posed a restriction on the thickness of the MXenes and limited their performance in volumetric energy storage. This issue can be addressed by introducing an optimized electrode architecture to enhance the charge/mass transport dynamics.[117]

The functionalization engineering endows a flexible and tunable bandgap of the MXene. The functionalization not only renders a high conductivity of the MXene to reduce the self-discharge effect but also

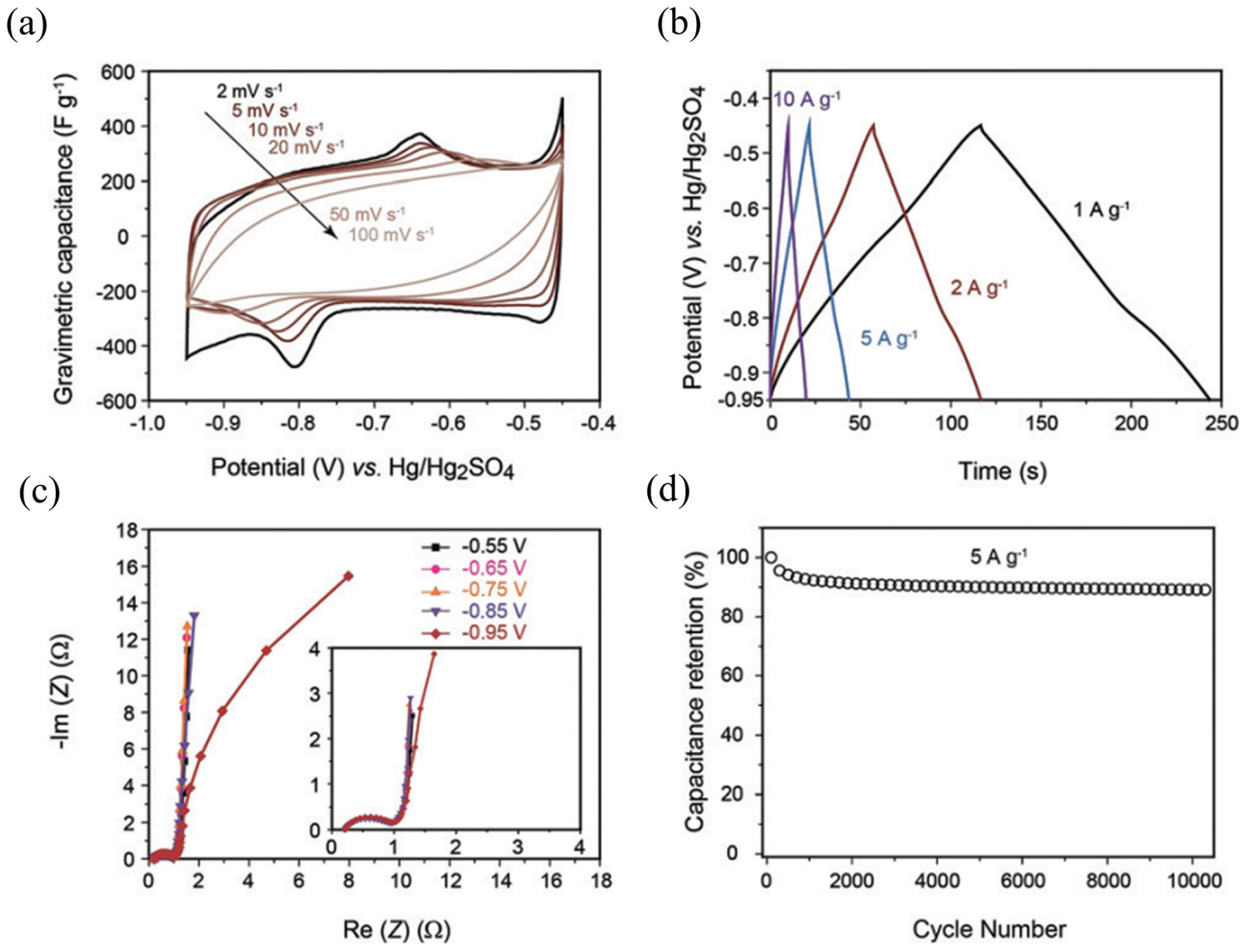

FIG. 7. Supercapacitor performance of the $Ti_3C_2T_x$ film electrode. (a) CV curves for the $Ti_3C_2T_x$ film electrode collected at 2, 5, 10, 20, 50, and 100 mV/s, respectively. (b) Galvanostatic charge/discharge (GCD) cycling profiles of the $Ti_3C_2T_x$ film electrode carried out at 1, 2, 5, and 10 A/g, respectively. (c) The EIS data collected at different potentials, while the inset shows the high frequency range. The Nyquist plots at 0.95 V showed a linear increase with a slope of different redox peaks in (a). (d) Capacitance retention test performed at 5 A/g.[58] Reproduced with permission from Li *et al.*, Angew. Chem., Int. Ed. **57**, 6115–6119 (2018). Copyright 2018 Wiley-VCH.

manifests a fortified pseudocapacitive active species at the MXene surface.[42]

In stark contrast with the HF-etched MXene, the F-termination free MXene holds an enriched oxygen termination. For electrochemical etching, the etching and termination processes are described as follows:

$$Ti_3AlC_2 - 3e^- + 3Cl^- \rightarrow Ti_3C_2 + AlCl_3, \quad (6)$$

$$Ti_3C_2 + 2OH^- - 2e^- \rightarrow Ti_3C_2(OH)_2, \quad (7)$$

$$Ti_3C_2 + 2H_2O^- \rightarrow Ti_3C_2(OH)_2 + H_2. \quad (8)$$

By combining the E-etching and intercalation processes, monolayer or bilayer MXene can achieve a high yield of 90%, which is comparable to or surpassing that achieved by the MXene made from the traditional method via direct or indirect HF etching. Owing to its enriched -O/OH functional groups and enlarged surface area, the promising applications of F-free MXene as an electrochemical capacitor are demonstrated.[90,118]

The spontaneous and electrochemical intercalations of cations in MXene layers have been confirmed in 2013 by Gogotsi *et al.*[38] The study demonstrated the spontaneous intercalation of various cations such as Li^+, Na^+, K^+, and Mg^{2+} and Al^{3+} into the MXene layers. Calcination and intercalation are capable of expanding the interlayer spacing ($d_{interlayer}$). Attributed to an increase in the $d_{interlayer}$ value from 9.6 to 12.5 Å, the specific surface area was increased from 1.4 to 22.6 m^2/g.[119] The result indicated that the treatment enhanced the surface area and hence improved the capacitance from 244 to 517 F/g. Apart from the enlarged surface area of the MXenes, their architecture designs usually result in better electrochemical activity due to the optimized mass transport kinetics. Lukatskaya *et al.* proposed two distinct architecture designs for MXenes as a supercapacitor electrode.[117] For the microporous MXene electrode, the capacitance delivered up to 310 F/g at a sweep rate of 10 mV/s. For the hydrogel film electrode, the capacitance could increase up to 380 F/g as shown in Fig. 8. With an optimized lateral dimension, the hydrogel electrode showed enhanced conductivity and ion accessibility, contributing to a high capacitance

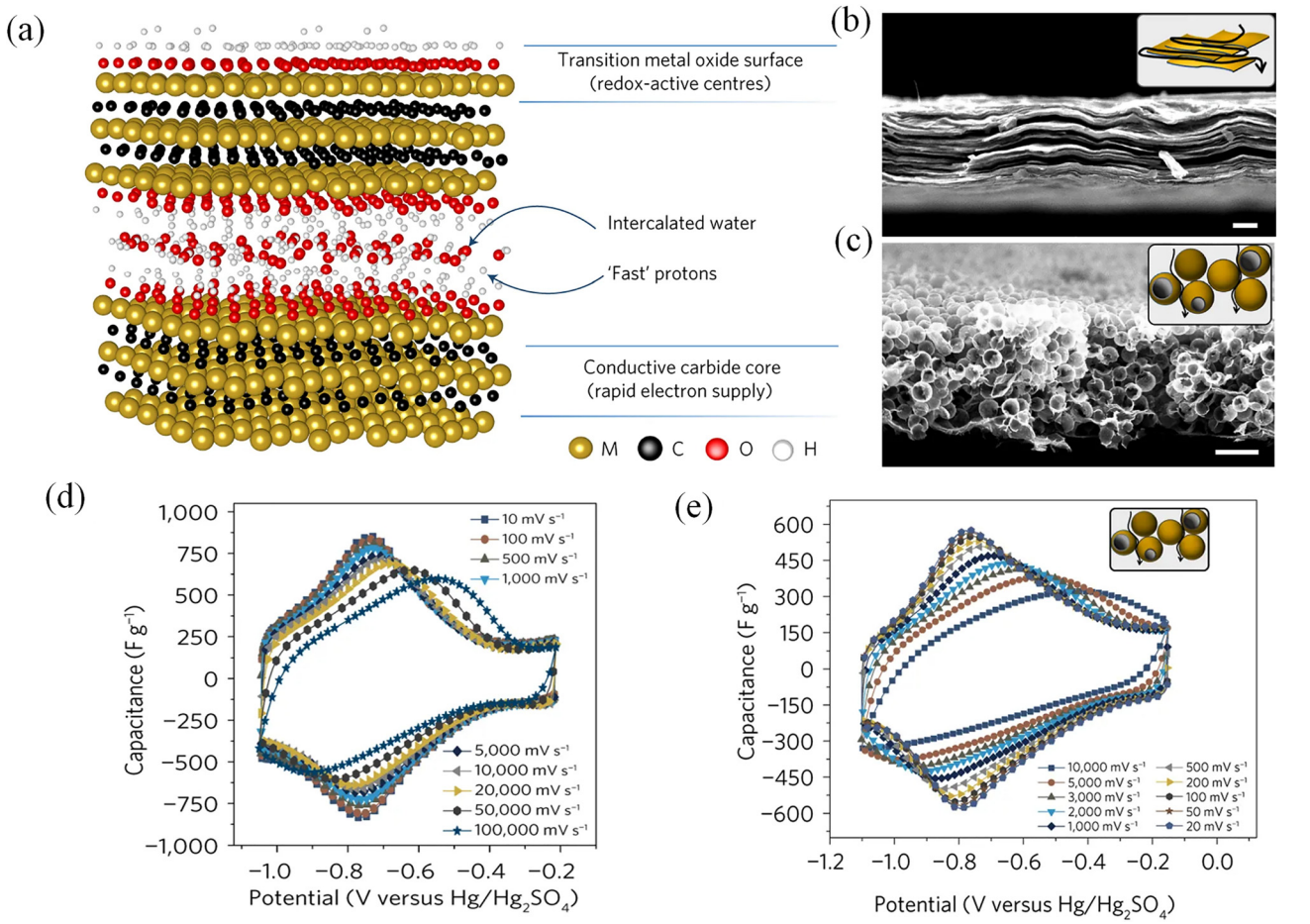

FIG. 8. (a) Schematic illustration of the MXene structure; the intercalated water molecules enable high accessibility of protons to the redox-active sites. (b) Scanning electron microscopy SEM image of hydrogel and (c) microporous templated $Ti_3C_2T_x$ cross section. (The insets show schematically the ionic current pathway in electrodes of different architectures.) CV data collected at scan rates (d) from 10 mV to 100 V/s for 90-nm-thick $Ti_3C_2T_x$ and (e) from 10 mV to 10 V/s for macro-porous 13-μm-thick MXene.[117] Reproduced with permission from Lukatskaya *et al.*, Nat. Energy **2**, 17105 (2017). Copyright 2017 Springer Nature Publishing.

of 435 F/g at a scan rate of 2 mV/s.[120] Furthermore, Chang *et al.* designed a flexible MXene capacitor by controlling the crumpling, which constituted indifferent dimensions.[121] The surface engineering on the MXene wrinkles successfully increased its mechanical strength by threefold, and the samples achieved a capacitance of 118 F/g at a scan rate of 1 A/g with good flexibility.

Motivated by the miniaturization of flexible wearable electronics, increasing efforts have been invested in the development of 1D fiber shaped supercapacitors. Fiber-shaped supercapacitors not only have high electrical conductivity but also promise energy storage applications. By the facile one-step wet-spinning approach, the fiber with a record conductivity of 1489 S/cm was synthesized by hybrid formulations of $Ti_3C_2T_x$ and poly(3,4-ethylenedioxythiophene):polystyrene sulfonate.[122] The hybrid fiber exhibits a high volumetric capacitance of 614.5 F/cm^3 at a scan rate of 5 mV/s and demonstrates its facilitating application as a supercapacitor to turn on a red LED over 30 s. By the polymerization of the 2D MXene to polyacrylonitrile (PAN) and the carbonization of the fiber network, the fiber mat composite electrode prevented the material delaminating from the substrate during folding or bending and maintained high stability and durability.[123] The electrospun MXene/carbon nanofiber exhibits an areal capacitance of 239 mF/cm^2 at a sweep rate of 10 mV/s and reveals a high retention of 100% over 10 000 cycles. Furthermore, the composite of the 1D cellulose nanofibrils and the robust MXene exhibits their stable colloidal dispersion with an improved pseudocapacitive activity.[124] The MXene/CNF composites hold a high mechanical strength of 341 MPa while maintaining a high capacitance of 298 F/g at a scan rate of 2 mV/s. The texturing technique showed that MXenes were able to fit into a highly stretchable architecture, showing attractive applications in wearable electronic devices.

Although MXenes have been explored to be promising electrochemical capacitors, their capacitive mechanism is dominated by the redox processes, which probably worked against by the double layer charges due to the charge dynamics between the surface and the electrolyte.[42] The introduction of electrochemically active materials into MXenes may provide a potential solution to this problem. For example, by introducing polymeric carbon nitride (p-C_3N_4) to the MXene, p-C_3N_4 serves as a nitrogen source and an intercalant. p-C_3N_4@Ti_2CT_x delivered a high capacitance of 327 F/g with 96.2% retention after 5000 cycles.[125] In addition to the introduction of the nitrogen source, the O dopant on the MXene enables the boosted effect of the Ti_3C_2 MXene. The N, O co-doped C@ Ti_3C_2 composites have been fabricated by an *in situ* polymerization method with the purging of the mixture of Ar and NH_3 gases at an annealing temperature of 600 °C. With the synergic effect of the abundant O- and N-functional group grafted carbon core and the high conductivity of the MXene, additional pseudocapacitance is provided by the extra ion adsorption. As a result, the co-doped supercapacitor manifests a high gravimetric capacitance of 250.6 F/g at a high current density of 1 A/g, maintaining a high retention of 94% after 5000 cycles.[126] Furthermore, the decoration of the pseudocapacitive species on MXene offers an improvement in energy storage by the hybrid energy storage mechanism of EDLC and redox-based pseudocapacitance.[127] Through the linking of silver nanowire ink and the electrochemically active RuO_2, the volumetric capacitance of the MXene raises from 76.8 to 821 F/cm^3 at a scan rate of 5 mV/s, demonstrating an 11-folded elevated enhancement in the capacitance.

Taking advantage of the anticipating high-volumetric-capacitance feature, MXene endows its emerging use as an electrochemical capacitor. Nevertheless, the relatively narrow potential window restricts the practical application as an all-solid-state supercapacitor. In the light of the hybrid system of redox-active hydroquinone/CNT and MXene, the asymmetric supercapacitor can operate in a high potential window of 1.6 V with a specific capacitance of 1080 F/g at a scan rate of 2 mV/s.[128] 2D metal-porphyrin frameworks (MPFs) have received attention in the application of advanced energy storage devices. However, the inferior conductivity and insufficient stability of the MPFs hinder their use in flexible free-standing electrodes. A new strategy of the utilization of the hydrogen bond by vacuum-assisted filtration technology is applied to address the intrinsic defect of the MPFs.[129] The resultant MXene/MPF frame affords a 3D interconnect conductive network, attributed to an enhanced pseudocapacitor by the accelerated ionic/electronic transport rate. The hybrid firm can stably deliver a capacitance of 326.1 F/g at a current density of 0.1 A/g over 30 000 cycles and manifest an areal capacitance of 408 mF/cm^2 with a capacitance retention of 95.9% after 7000 cycles as a symmetric supercapacitor. The carbon-based material endows a robust structure and resistance-reduced backbones to the MXene. Recently, it was proposed that a bonded activated carbon (AC) as an electrochemically active material for EDLC storage could be linked to the MXene with reduced graphene oxide (r-GO) and therefore formed a sandwich layer of the MXene-rGO-AC structure.[130] This composite constructed a 3D electrode network for a supercapacitor electrode, which exhibited a gravimetric capacitance of 126 F/g at a current density of 0.1 A/g. The MXene/graphene based composite all-solid-state supercapacitor devices were fabricated, which demonstrated an excellent volumetric capacitance up to 216 F/cm^3 at a current density of 0.1 A/cm^3. In addition, the flexible supercapacitor devices also exhibited a significant areal capacitance up to 3.26 mF/cm^2 and a volumetric capacitance up to 33 F/cm^3 at a current density of 2 mV/s, which are larger than those of the reported graphene-based micro-supercapacitors.[131]

C. 2D TMD/MXene composites

The hybrid composites with two or more materials can be constructed, which are able to combine the merits of individual counterparts and optimize their properties. In addition, the composites generate multifunctional applications and modulate their physical and chemical properties, which may obtain better performance in the field of specific applications.[12]

MoS_2 is the typical type of TMD, which is easy to be intercalated and modified due to its unique structure. $Ti_3C_2T_x$ is the common type of MXene, which may possess superior electrochemical properties, benefited from its extremely metal conductivity, hydrophilic characteristics, and pseudo-capacitance working mechanism. Therefore, the $MoS_2/Ti_3C_2T_x$ composite can effectively improve the electrochemical properties, for instance, a higher specific capacitance of the composite than those of pure MXenes. The maximum specific capacitance of the MoS_2/MXene composite based micro-supercapacitors is 173.6 F/cm^3 at a current density of 1 mV/s, and the maximum energy density and power density are 15.5 mWh/cm^3 and 0.97 W/cm^3, respectively. In addition, the micro-supercapacitors demonstrate the excellent cycle stability and flexibility.[132]

The hybrid structure opens up a new possibility to the MXene to overcome the pristine with relatively low capacitance and also enlarged

the potential window of the supercapacitor, leading to broad applications in the energy storage.

IV. TMDs AND MXenes FOR ELECTROCATALYS

With the growing awareness in the energy crisis and the continuous consumption of fossil fuel, search of clean energy is a surpassingly urgent issue in the past few decades.[140,141] Distinct from renewable energy such as wind energy,[142,143] hydrogen energy is considered as an alternative energy source, which is clean and environment-friendly.[144] Producing hydrogen fuel via water splitting is an effective way to provide hydrogen energy. The sustainable hydrogen production requires highly efficient and robust earth-abundant electrocatalysts for HER. Novel materials such as platinum and palladium have been successfully commercialized for wide use in electrocatalytic applications.[145] Limited by its low abundance and high cost, the novel metal based electrocatalysts restricted their use in fuel production and the promotion of the clean energy in extensive energy conversion applications.[146] On the other hand, the 2D material has a high surface-to-volume ratio and a shorten diffusion length, and it is considered as a promising substitution to the novel metal catalyst. Generally, the HER activity in the 2D material likely tends to occur in acidic media rather than the alkaline media due to the sluggish reaction in the water splitting process.[97] The water splitting and hydrogen evolution reaction are described by the following three key steps: electrochemically adsorption/desorption, dissociation/combination, and chemical desorption process, namely, Volmer, Heyrovsky, and Tafel reactions, respectively. The reactions can be written as the following equations and "M" represents the catalyst:

$$H^+ + e^- + M \rightarrow M - H, \quad (9)$$

$$M - H + M - H \rightarrow H_2 + 2M, \quad (10)$$

$$H^+ + M - H \rightarrow H_2 + M. \quad (11)$$

Since the reactions are closely related to the surface area of the catalyst "M," the electrocatalytic active site is detrimental to the HER activity. Advantageous from the 2D layered structure, the 2D material creates extra electrocatalytic active sites than the traditional bulk material.[36] The high electrocatalytic activity is attributable to the hydrogen adsorption characteristics.[147] For example, the Mo based 2D materials such as MoS_2 and Mo_2CT_x have been explored to promote the performance of HER, which is attributed to their basal electrocatalytic properties.[49,97] In order to reduce the production cost and lower the overpotential, various electrocatalytic materials and approaches have been studied and promoted by a number of academies, institutions, and researchers.[148–158] Here, some representative electrocatalytic materials are presented and summarized in Table II.

A. TMDs

TMDs have a large specific surface area and the intrinsic catalytic activity. In particular, the edges of MoS_2 were considered as active sites for the HER electrocatalyst. In addition, density functional theory (DFT) calculations indicated that the hydrogen adsorption energy on the edge of TMDs such as MoS_2 was estimated to be close to zero, indicating that MoS_2 may be an attractive HER electrocatalyst.[159] Jaramillo *et al.* demonstrated that the HER activity correlated linearly with the number of edge sites of MoS_2.[160] Many other 2D materials were also found to possess the HER activity with their active edge sites.[161] Therefore, constructing or exposing more active edge sites could be an effective strategy to improve the HER activity. Xie *et al.* showed engineering defects into MoS_2 to expose additional active edge sites via its unique defect-rich structure.[162] The defect-rich MoS_2 ultrathin nanosheets showed a small onset overpotential of 120 mV and a small Tafel slope of 50 mV/decade, which are better than those of the defect-free nanosheets (180 mV and 87 mV/dec) or the bulk materials (250 mV and 81 mV/dec).

Various strategies, such as defect engineering, doping, increasing active sites, and hybridization, could improve the HER activities.[149,150,163] A new type of defect- and S-rich ultrathin MoS_2 nanosheet with an N-doped carbon nanofiber composite structure (MoS_2/NCNFs) was reported,[164] exhibiting a small overpotential of 135 mV and a small Tafel slope of 48 mV/dec. The high HER activity of MoS_2/NCNFs may arise from the synergy of NCNFs and MoS_2 and defect- and S-rich, ultrathin MoS_2 structures. A phase transition from cubic to orthorhombic phases in $CoSe_2$ via phosphorus-doping was reported.[165] Noted that the orthorhombic $CoSe_2$ with an 8 wt. % phosphorus dopant showed the lowest overpotential of 104 mV at 10 mA/cm^2 in 1 M KOH, with an onset potential as small as 31 mV. In addition, a small Tafel slope of 69 mV/dec was achieved for phosphorus-doping $CoSe_2$, implying its excellent HER activity as compared to those of Pt/C and other documented HER single catalysts [Figs. 9(a) and 9(b)]. The optimization of the basal plane of monolayer 2H-MoS_2 for HER was carried out by introducing sulfur (S) vacancies and strain.[152] The theoretical and experimental results showed that the S-vacancies were new catalytic sites in the basal plane [Fig. 9(c)]. The overpotentials for unstrained S-vacancy MoS_2 (V-MoS_2) of 250 mV and strained S-vacancy MoS_2 (SV-MoS_2) of 170 mV were obtained at a current density of 10 mA/cm^2, as shown in Fig. 9(d). The corresponding Tafel plots showed that strain decreased the Tafel slope from 98 to 90 mV/dec, whereas S-vacancies reduced the Tafel slope from 98 to 82 mV/dec. In contrast, combining strain and S-vacancies decreased the Tafel slope to 60 mV/dec. Such a Tafel slope had been observed for Mo_3S_{13} clusters, which was ascribed to a chemical rearrangement before H_2 desorption became the rate-limiting step. It was reported that $MoSe_2/MoO_2$ hybrid nanosheets with an abundant edge and high electrical conductivity were synthesized on the surface of Mo foil by introducing a layer of MoO_2 on Mo foil.[166] Metallic MoO_2 could improve the charge transport efficiency of $MoSe_2/MoO_2$, thereby enhancing the overall HER performance. $MoSe_2/MoO_2$ exhibited fast hydrogen evolution kinetics with a small overpotential of 142 mV at a current density of 10 mA/cm^2 and a Tafel slope of 48.9 mV/dec, as shown in Fig. 9(e). The electronic structure of active edge sites of Se in $MoSe_2$ could be modulated by electron injection from ruthenium deposited on $MoSe_2$ nanosheets.[167] The Rh–$MoSe_2$ nanocomposite exhibited great performance enhancement with a low onset potential of 3 mV and a quite low overpotential of 31 mV, which are superior to those of almost all Rh-based and $MoSe_2$-based electrocatalysts [Fig. 9(f)].

Metallic TMDs exhibit a low charge-transfer resistance, which could improve the HER performance. Flower-like MoS_2 sheets with a high density of exposed edges were grown using chemical vapor deposition, and the as-grown 2H–MoS_2 was converted to 1T-MoS_2 via the lithium intercalation method.[168] 1T–MoS_2 showed an enhanced HER activity with a low overpotential of 187 mV and a small Tafel slope of 43 mV/dec compared to those of 2H–MoS_2. This is because the

TABLE II. Various 2D materials and their HER performances.

2D material category	Material	Onset overpotential (mV)	Overpotential @ 10 mA/cm^2 (mV)	Tafel slope (mV/dec)	References
TMDs	S-rich MoS_2	…	135	48	164
	1T-MoS_2	…	175	41	200
	1T-$MoSe_2$	60	179	78	175
	1T-$MoSe_2$	…	152	52	174
	$ReS_{2(1-x)}Se_{2x}$	32	84	50.1	172
	1T-WS_2	…	142	70	180
	1T-VS_2	…	43	36	181
	1T-VSe_2	70	126	59	182
	1T-WTe_2	…	…	57	184
	1T-TaS_2	106	196	85	185
	MoSSe	49	140	40	171
	ReS_2	…	147	69	170
	Rh–$MoSe_2$	3	31	40	167
	P-doping $CoSe_2$	31	104	69	165
	$MoSe_2$/SWCNTs	…	100	63	176
	$MoSe_2/MoO_2$/Mo	60	142	48.9	166
MXenes	Mo_2CT_x	…	283	82	100
	Ti_2CT_x	…	609	138	100
	Ti_2CT_x	…	170	100	98
	Co^{3+}-Cr_2CT_x	…	425	112	90
	CoP@MXene	220	298	58	196
	NiFe-LDH/MXene/NF	190	229	44	197
	$Ti_3C_2T_x$	75	169	97	198
	Pt/$Ti_3C_2T_x$-550	…	32.7	32.3	199
	$Pt_xNi@Ti_3C_2T_x$	…	18.55	13.37	200
	TBA-$Ti_3C_2T_x$-Pt-20	…	55	65	201
	Ru_{SA}–N–S–$Ti_3C_2T_x$	~0	76	90	202
	P3-V_2CT_x	28	163	74	203
	Co–MoS_2/Mo_2CT_x	…	112	82	205
	$TiO_2C@CN_{x,950}$	…	254.5	60	207
Black phosphorus	$MoSe_2$–BP	200	380	97	208
Graphene	Co@N-doped graphene	13	70	64	209
LDH	Ni–Mn–LDH/g-C_3N_4	…	147	50	210

metallic 1T–MoS_2 exhibits a low charge-transfer resistance relative to that of the as-grown 2H–MoS_2. It was shown that the high purity 2D layered metallic-phase 1T′-MoX_2 (X = S, Se) bulk crystals could be synthesized.[169] A remarkable HER performance on the basal plane of 1T′-MoS_2 was observed, with an onset overpotential of 65 mV and an overpotential of 400 mV at a current density of 607 mA/cm^2, which is among the best in MoS_2-based electrocatalysts, as shown in Figs. 10(a) and 10(b). Such an excellent HER performance originates from the higher catalytic activity on the basal plane and better charge transport character of 1T′-MoS_2 compared to 2H–MoS_2. In addition, high electrocatalytic HER activity was found in 1T′-ReS_2 with a low overpotential of 147 mV at a current density of 10 mA/cm^2,[170] which exceeds that of MoS_2 through the activation/optimization technique, exhibiting the charge engineering optimizing effect of the Re–Re bond [Figs. 10(c) and 10(d)]. Noted that a general and facile method is demonstrated for high-yield, large-scale production of 1T-phase single-layer TMD nanodots with high-density active edge sites and clean surface, including MoS_2, WS_2, $MoSe_2$, $Mo_{0.5}W_{0.5}S_2$, and MoSSe. The proposed method gave rise to a significant enhancement in electrochemical HER performances as compared to their corresponding nanosheets.[171] Impressively, the obtained MoSSe nanodots may result in a low overpotential of 140 mV at a current density of 10 mA/cm^2, a Tafel slope of 40 mV/dec, and excellent long-term durability. The experimental and theoretical results suggest that the excellent catalytic activity of MoSSe nanodots is resulted from the high-density active edge sites, high-percentage metallic 1T phase, alloying effects, and basal-plane Se-vacancies

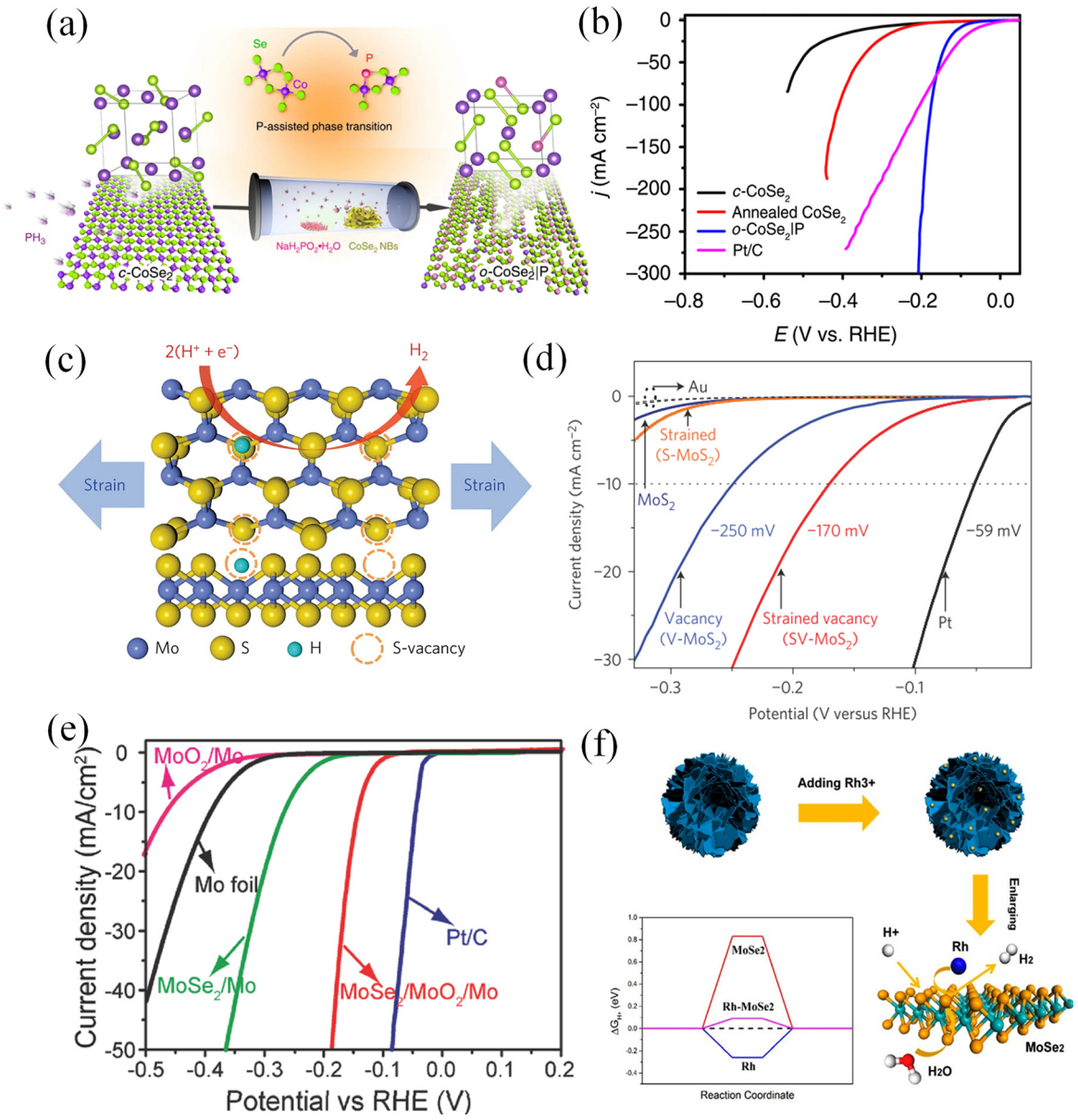

FIG. 9. (a) Schematic illustration of the P-assisted phase transition from cubic phase $CoSe_2$ to orthorhombic phase $CoSe_2|P$ through an annealing process. Violet, green, and pink balls correspond to Co, Se, and P atoms, respectively. (b) Polarization curves for the HER on c-$CoSe_2$, annealed c-$CoSe_2$, o-$CoSe_2|P$, and commercial Pt/C.[165] Reproduced with permission from Zheng *et al.*, Nat. Commun. **9**, 2533 (2018). Copyright 2018 Authors, licensed under a Creative Commons Attribution 4.0 (CC BY) International License. (c) Schematic of the top (upper) and side (lower) views of MoS_2 with strained S-vacancies on the basal plane. (d) Individual and combined effects of elastic tensile strain and S-vacancies on the HER activity of monolayer MoS_2.[152] Reproduced with permission from Li *et al.*, Nat. Mater. **15**, 48–53 (2016). Copyright 2016 Springer Nature Publishing. (e) The polarization curves of $MoSe_2/MoO_2/Mo$, $MoSe_2/Mo$, MoO_2/Mo, Mo foil, and commercial Pt/C.[166] Reproduced with permission from Jian *et al.*, Small **14**, 1703798 (2018). Copyright 2018 Wiley-VCH. (f) Schematic illustration of the synthesis process of the Rh–$MoSe_2$ nanocomposite.[167] Reproduced with permission from Liu *et al.*, ACS Sustainable Chem. Eng. **6**, 9137–9144 (2018). Copyright 2018 American Chemical Society.

[Fig. 10(e)]. A series of 1T′-phase $ReS_{2x}Se_{2(1-x)}$ ($x = 0$–1) nanodots were synthesized to achieve high-performance HER in acid medium by combining chemical vapor transport and Li-intercalation.[172] The 1T′-phase ReSSe nanodot exhibited high hydrogen evolution activity, with a low overpotential of 84 mV and a Tafel slope of 50.1 mV/dec at a current density of 10 mA/cm^2. The excellent hydrogen evolution activity is relevant to the optimal hydrogen absorption energy of the active site induced by the asymmetric S vacancy in the highly asymmetric 1T′ crystal structure, as shown in Fig. 10(f).

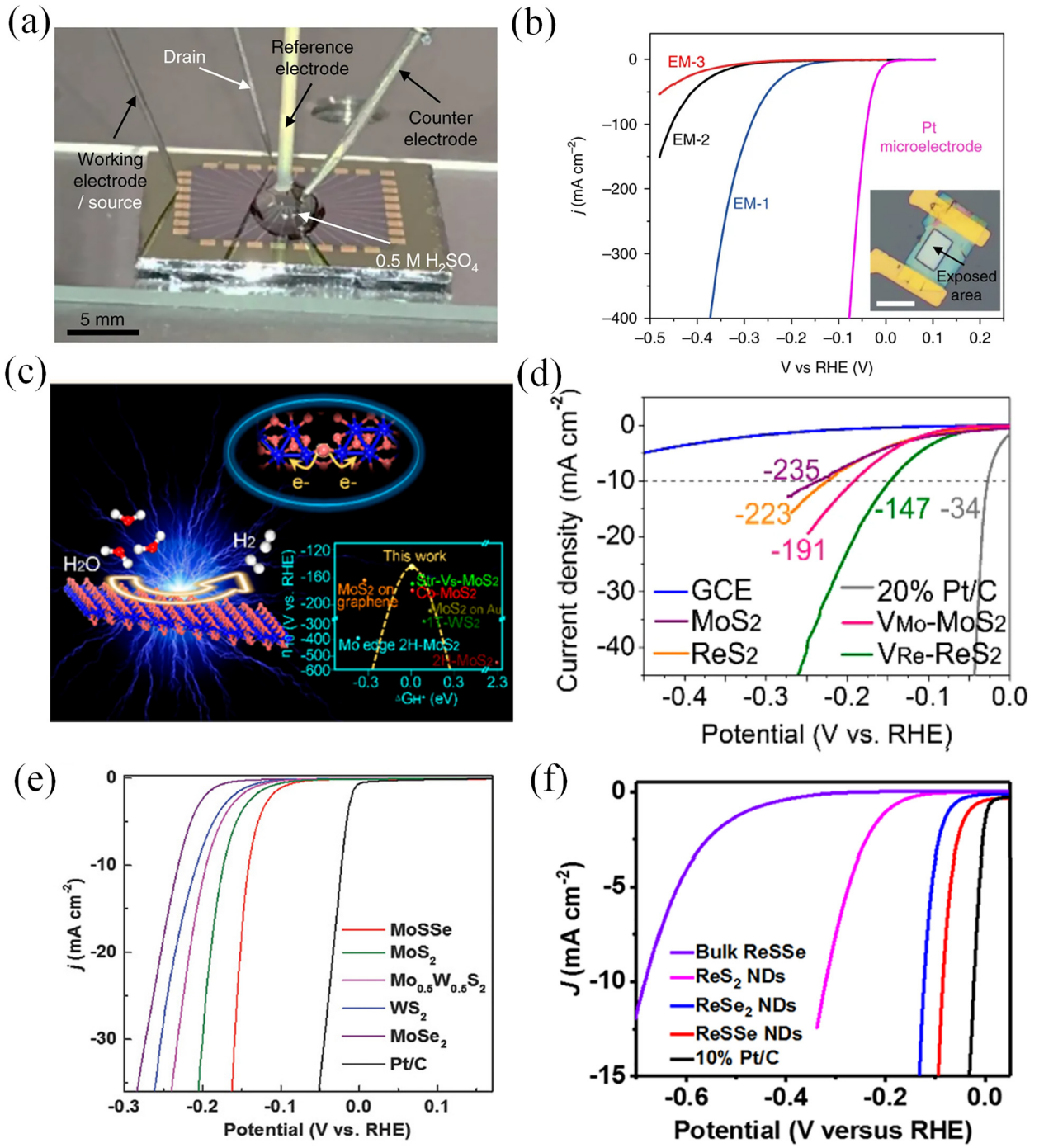

FIG. 10. (a) Photograph of the electrochemical setup for electrocatalytic HER measurements. (b) Polarization curves of electrochemical microcells (EM-1, EM-2, and EM-3); the inset shows the optical microscopy image of EM-1. The scale bar is 20 μm.[169] Reproduced with permission from Yu *et al.*, Nat. Chem. **10**, 638–643 (2018). Copyright 2018 Springer Nature Publishing. (c) Comparison of η_{10}-ΔG_{H*} for TMDs with sole activation and optimization by varied techniques. (d) Polarization curves of V_{Re}-ReS_2, V_{Mo}-MoS_2, ReS_2, MoS_2, glass carbon electrode, and commercial Pt/C.[170] Reproduced with permission from Zhou *et al.*, ACS Nano **12**, 4486–4493 (2018). Copyright 2018 American Chemical Society. (e) Polarization curves of MoSSe, MoS_2, $Mo_{0.5}W_{0.5}S_2$, WS_2, $MoSe_2$ nanodots, and commercial Pt/C.[171] Reproduced with permission from Tan *et al.*, Adv. Mater. **30**, 1705509 (2018). Copyright 2018 Wiley-VCH. (f) Polarization curves of the bulk ReSSe, ReS_2, ReSSe, $ReSe_2$ NDs, and commercial Pt/C.[172] Reproduced with permission from Lai *et al.*, J. Am. Chem. Soc. **140**, 8563–8568 (2018). Copyright 2018 American Chemical Society.

Other TMD materials such as WSe_2,[173] $MoSe_2$,[174–177] $MoS_{2(1-x)}Se_{2x}$,[178] WS_2,[179,180] VS_2,[181] VSe_2,[182] CoS_2,[183] WTe_2,[184] TaS_2,[185] $PdTe_2$,[186] and $PtTe_2$[186] have also been found to be active for electrocatalytic HER.

B. MXenes

Taking advantage of the special catalytic property on the basal planes, a new and intriguing family of 2D transition metal MXene has been adopted as a promising electrocatalyst. Efforts and improvements have been invested in surface engineering, and the electrode design was theoretically and experimentally evidenced by their improvement theoretically and experimentally. Seh *et al.* conducted a computational screening study of 2D layered Mo_2CT_x and Ti_2CT_x by DFT.[100] With the combination of experimental synthesis and theoretical calculation of Mo_2CT_x, it suggested that basal planes of Mo_2CT_x were catalytically active in HER. The unique electrocatalytic characteristics are different from the TMDs. For example, HER likely occurred at the edge sites of the 2H phases of MoS_2; thus, the characteristics render a special electrocatalytic activity for MXene in HER.[187,188] Moreover, Pandey *et al.* used DFT to investigate the combined stability and activity analysis of 72 different MXenes and anticipate the nonprecious MXenes (e.g., Cr_2CO_2, $Cr_4C_3O_2$, and Nb_2NO_2) as promising candidates for HER electrocatalysts.[189] For most of the MXenes, except Ti-based MXene, the F-functional group exhibited less favorable stability under HER conditions. On the other hand, the effect of the oxidation process is generally positive for the HER activity of the MXene, excluded from W-based MXenes whose HER activity was degraded due to the oxidation process.[190]

Introducing transition metals[191] and N-doped graphene[192] into MXene is considered as an efficient strategy to lower the Gibbs energy for HER activity. Promoters (Ni, Co, and Fe) are capable of lowering the H–O bonding on the MXene effectively, and the ions attached to different active sites result in a diverse ΔG_H. The most optimized atomic dispersion on vanadium carbide is one TM ion on the top site of surface O atoms connected to 3 V atoms. The calculation also suggested that promoters could sufficiently increase the number of electrons that donated the O atoms. Benefited from the large Bader charge of TM-V_2CO MXene, the electrons from TM will take the σ^* occupancy, resulting in a weakened H–O bond and lowered ΔG_H value. Very recently, our group developed a universal method to synthesize HF-free MXenes [Fig. 11(a)] and demonstrate their electrocatalytic activity.[90] The research first depicts the relationship between electrocatalytic activity and the pseudo-capacitance, where the capacitive

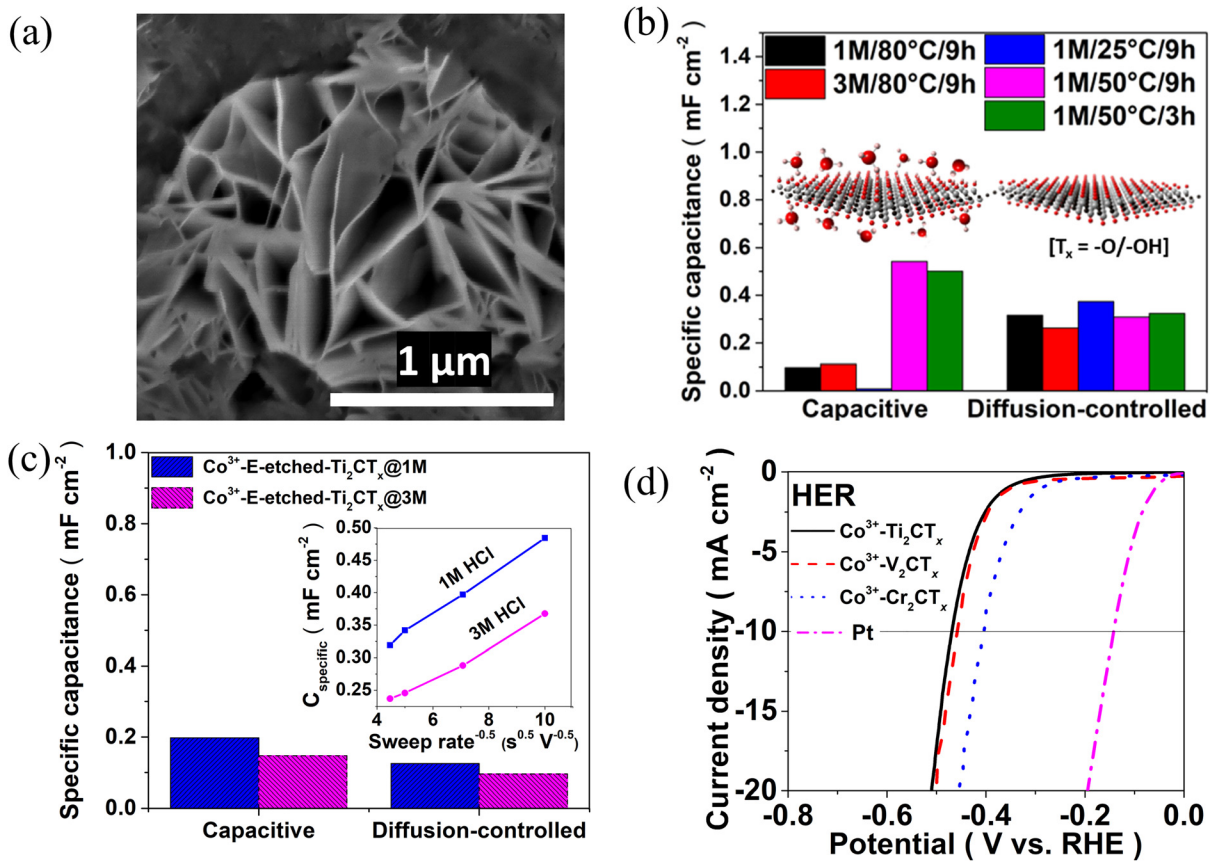

FIG. 11. (a) High-magnification SEM images of the HF-free MXene. (b) The kinetics analysis of the various HF-free Ti_2CT_x MXenes as a mechanism study. (c) The contribution of the capacitive and diffusion-controlled capacitance of Co^{3+}-Ti_2CT_x for HER. (d) The anodic-going iR corrected linear sweep voltammetry (LSV) of Co^{3+}-MXenes for HER activity.[90] Reproduced with permission Pang *et al.*, J. Am. Chem. Soc. **141**, 9610–9616 (2019). Copyright 2019 American Chemical Society.

capacitance affects the HER activity directly due to the hydrogen coverage [Fig. 11(b)]. By the synergetic effect of the Co^{3+} ions and the pristine electrochemically etched MXene, the HER overpotential of the TM ion terminated electrocatalyst is effectively reduced by 110 mV [Figs. 11(c) and 11(d)]. The work opens up an opportunity of the HF free MXene on the electrocatalytic application. Nonetheless, further investigation of the working mechanism of the HF-free MXene is needed along with the desired optimization on the synthesis method for the later research.

With high electrical conductivity, hydrophilicity, porosity, and stability, the functionalized-MXenes possess widespread applications in energy storage.[193,194] However, intersheet aggregation found in the MXenes via vdW force and hydrogen bonds[195] may restrict their functionalities, processability, and performance in MXene-based materials/devices. Therefore, MXene with a unique 3D architecture (3D Ti_3C_2-MXene) was fabricated by ultrasonic atomization of the MXene colloidal solution into aerosol droplets[196] such that the active surface area, charge-transfer kinetics, and mass diffusion rate of the 3D Ti_3C_2-MXene were efficiently increased. The 3D Ti_3C_2-MXene was also coupled with the CoP nanocrystal and had a good HER activity with a low overpotential of 298 mV at a current density of 10 mA cm^{-2}. The boosting effect of the 3D architecture is evidenced for the MXene [Fig. 12]. Beneficial from their hierarchically porous structure and the hydrophilic feature, the microporous 3D MXene framework is capable of conjugating to the nickel-iron layer double hydroxide and resulting in an accelerating hydrogen evolution at high current density.[197] Importantly, the synergetic effect facilitates the boosted ion transfer kinetics of the electrode and enables a fast discharge reaction Volmer reaction in the water spitting process. Taking advantage of the enhancing water adsorption/activation on the catalyst, the composite exhibits a low overpotential of 132 mV at a scan rate of 10 mV/s. Notably, the catalyst demonstrated a superior performance at a high current density of 500 mA/cm^2 at an overpotential of 205 mV, while the Pt/C catalyst required a higher overpotential of 366 mV. An appropriate architecture design not only enhances the coupling ability of the MXene but also achieves a favorable performance in HER activity. A novel method was proposed to prepare uniform MXene nanofibers by "shearing" the MAX phase materials with KOH first and then

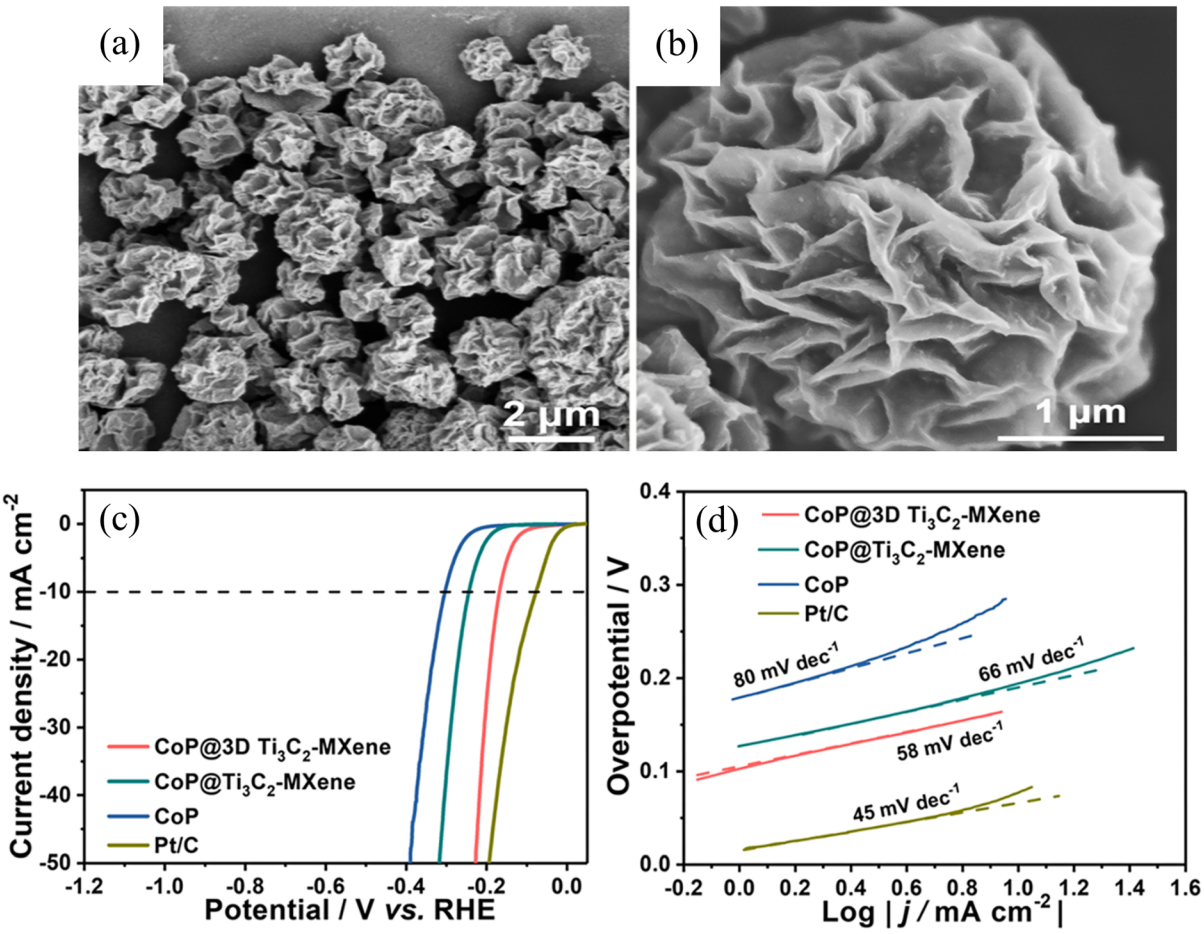

FIG. 12. (a) and (b) SEM images of the CoP@3D Ti_3C_2-MXene architecture. (c) The *i*R-corrected polarization curves and (d) Tafel plots of CoP@3D Ti_3C_2-MXene, CoP@Ti_3C_2-MXene, CoP, and Pt/C catalysts for HER.[196] Reproduced with permission from Xiu *et al.*, ACS Nano **12**, 8017–8028 (2018). Copyright 2018 American Chemical Society.

followed by HF etching.[198] The MXene nanofibers had a low overpotential of 169 mV at a current density of 10 mA cm^{-2}.

It is noted that the chemical and physical properties of MXenes largely depend on the surface functional groups. Recently, the Ti_2CT_x nanosheet with rich F-termination was prepared by annealing in vacuum to remove -O/-OH groups (Fig. 13).[98] With reduced charge-transfer resistance and subsequently boosted electrode kinetics toward HER, these annealed-Ti_2CT_x nanosheets had a lower onset potential and reached a specific current density of 10 mA cm^{-2} at 170 mV, in comparison to the alkalized-Ti_2CT_x nanosheets (with lower -F coverage). Moreover, the DFT calculation suggested that the increase in terminated F atoms not only decreased ΔG_H, an effective descriptor of HER performance, but also increased the proton adsorption kinetics, which showed the promises of MXene in HER.[98] These works thus provide new insights into the functional group-induced properties of the MXene and establish a solid framework to the application of functionalized-MXene in hydrogen evolution.

C. Composites

Coupling between the electrocatalytic active material and MXene is an essential strategy to boost the HER activity. Recently, the *in situ* Pt_3Ti nanoparticles on 2D MXene are employed to provide an extensive study on the effect of the novel metal in MXene.[199] A facile annealing route was adopted instead of the traditional chemical co-reduction method used to overcome the challenge for the synthesis of Pt-based intermetallic compounds. Followed by the comprehensive investigation of the temperature and the composite ratio, Pt/$Ti_3C_2T_x$-550 holds an exceptional catalytic performance for HER. Accordingly, the catalyst exhibits a low overpotential of 32.7 mV at a current density of 10 mA/cm^2 with a small Tafel slope of 32.3 mV/dec. Atomic coupling of the novel metal on the MXene may not only reduce the cost but also hold the benefits of the shorten diffusion length of the nanomaterial. Coupling the PtNi nanowire to the MXene offers more active sites and exhibits a record-breaking performance of low overpotential of 18.55 mV with a small Tafel slope of 13.37 mV/dec.[200] Direct introduction of the Pt nanoparticles at the atomic scale contributes a

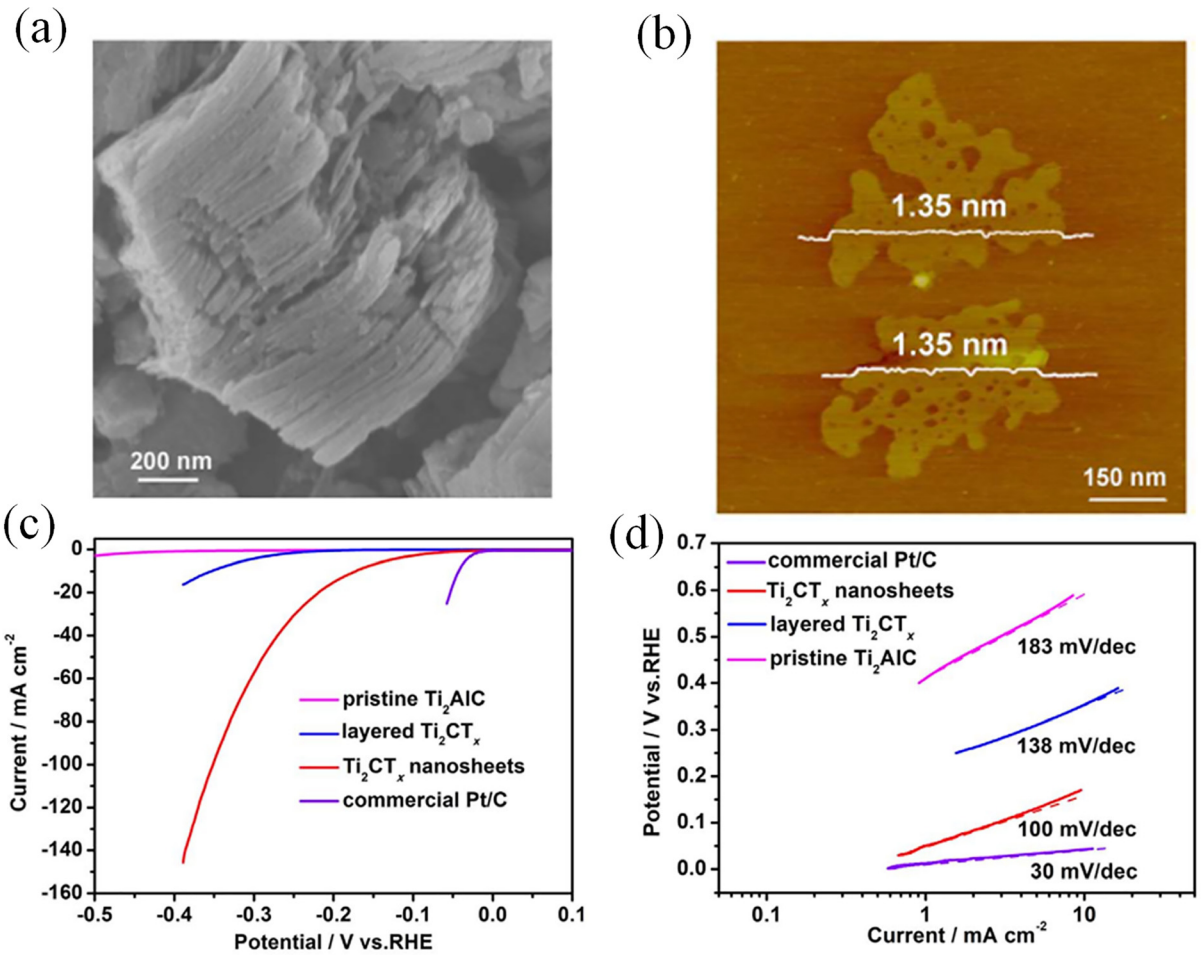

FIG. 13. (a) The SEM and (b) atomic force microscopy image of the layered Ti_2CT_x. (c) The LSV curves for Ti_2CT_x with different morphologies and (d) the corresponding Tafel plots.[98] Reproduced with permission from Li *et al.*, Nano Energy **47**, 512–518 (2018). Copyright 2018 Elsevier.

promising catalytic activity in HER.[201] Taking the negatively charged TBA treated MXene nanosheet as a support, the interaction through the electrostatic force can provide a uniform distribution of Pt. By means of treatment of the wet impregnation and the photo-induced reduction process, TBA-$Ti_3C_2T_x$-Pt-20 manifests an overpotential of 55 mV at a current density of 10 mA/cm^2 corresponding to a low Tafel slope of 65 mV/dec. Owing to the coupling favorable ability, MXene serves as a host to a ruthenium single atom catalyst with coordinated with nitrogen and sulfur elements.[202] With the combination of the structural spectroscopy and the TEM investigation, the atomic dispersion of Ru on MXene is revealed, rendering a superior activity toward the HER. Accordingly, the Ru_{SA}-N-S-$Ti_3C_2T_x$ catalyst exhibits a low overpotential of 76 mV and achieves a current density of 10 mA/cm^2.

Adjacent to the utilization of the precious metal (e.g., Pt), the heat treatment with a polymer of triphenylphosphine (TPP) also provides an impressive enhancement in the HER activity. The phosphorous species lower the Gibbs free energy of the MXene to manifest a low overpotential of 163 mV at a specific current density of 10 mA/cm^2 with a Tafel slope of 74 mV/dec.[203] Through theoretical calculation and experimental investigations, the contacting of MoS_2 to MXene is evident to vanish the p-type Schottky barrier and result in an enhanced HER.[204] By the *in situ* conversion of MoS_2 on the Co-doped Mo_2CT_x MXene, the novel Co-MoS_2/Mo_2CT_x shows a low overpotential of 112 mV at a current density of 10 mA/cm^2 along with a long-term stability of 18 h in alkaline media.[205]

The graphene/Ni_3Se_2/Co_9S_8 composite was constructed owing to the advantage of the novel 3D hybrid structure, large surface area, highly conductive graphene support, and synergistic effect. The composite exhibits outstanding electrocatalytic activity with an overpotential of 0.17 V at a current density of 20 mA/cm^2. According to the experimental results and theoretical calculations, the excellent electrocatalytic activity of the graphene/Ni_3Se_2/Co_9S_8 composite results from the unique 3D hierarchical structure, coupling interactions, and interface reconstruction, which causes the lower energy barrier of hydrogen desorption for the water splitting.[206]

V. SUMMARY AND PERSPECTIVES

Great efforts have been devoted to the design and construction of TMD and MXene based advanced electrode materials for developing high-performance electrochemical energy storage and conversion devices. Electrochemical energy devices in terms of supercapacitor and water splitting are a rapidly evolving thrust area where these materials show great potential to compete with the traditional energy materials. Specifically, the relevant properties of MXenes for energy storage and conversion applications can be optimized by the control of concentration of the etchant, selections of architecture design, and composites. The electrochemical behavior of MXene can be adjusted by modifying the concentration of the etchant determining the interlayer water and functional groups (-O, -OH, and -F). A rich -F terminated MXene shows an enhanced HER activity when compared to the -O/-OH rich MXene. The architecture design with a large surface area may provide more active space on the MXene, and accordingly, the design can improve the HER activity and electrochemical capacitance of the MXene. However, the limited ion accessibility and the restricted active site may hinder the development of the pristine 2D material. Furthermore, the combination of a 2D material with a large volume material can effectively prevent the restack issue of the 2D material. Thus, a synergistic effect of large area architecture and coupling an electrochemically active material (CoP, activated carbon and p-C_3N_4) to the MXenes can lower the overpotential of the MXene catalyst at a specific current density and hence increase the gravimetric/volumetric capacitance. Aside from the -F-based etching method, the alkali-assisted hydrothermal and electrochemically etching methods of producing MXene from the MAX phase have also shown a successful extraction of the "A" layer. Such novel -F free synthesis methods not only pave the way for producing MXene via a non-toxic route but also bring challenges with tunable surface terminations. Additionally, new 2D materials with different atomic arrangements and compositions, such as order double MXene, are not fully investigated at the current stage. The later investigations may provide an opportunity for new device and electrochemical applications.

Still, there are some underlying surface-kinetics related mechanisms, which are unclear and desirable for further study. Using the combination of the theoretic calculation such as DFT and experiment investigations, the challenge on the development of 2D material-based devices is to be alleviated. Thus, further investigations in understanding the electrochemical mechanism and controlling the ion transfer kinetics are urgently needed to achieve a high-power supercapacitor and efficient electrocatalysis for water-spitting. Such approaches offer a practical guide for improving the performance and exploring possible composites for TMD and MXene supercapacitors and electrocatalysts. On the other hand, 2D materials have demonstrated enormous promising applications for high-performance electrochemical energy devices, such as 2D transition metal oxides/hydroxides, single-element 2D materials, and 2D conductive polymers. The selection from the booming combinations is vital for the expanding study on the 2D material. Hence, the formed composites with the combination of these 2D materials may collect their respective merits, which could provide a solution for the development of 2D materials in high-performance electrochemical energy device applications.

Nevertheless, concerns are aroused due to the rapidly expanding study on the 2D material hybrid.[211] To avoid one-way development of combining 2D materials with electrochemically active materials, researchers need to consider a novel pathway of enhancing pure 2D materials and investigation of the underlying mechanism. On the other hand, engineering on the pristine 2D material is essential for alleviating the common issue of the vdW force driven restack of the 2D material. Inspiringly, the morphology engineering and the surface functional group modification for the non-treated 2D material have shown the advances in electrochemical properties according to our group's most recent report and other teams' earlier studies.[196,198,212] By the enhanced active site and double layer capacitance, the electrochemical performance reaches the highly desirable value, which is close to that obtained by the theoretical calculation. Such research advances not only reveal the new possibility of the pristine 2D material but also are inspirational to future research studies due to their universally applicable strategy. It is believed that the theoretical simulation and effective mechanism study on the 2D material will facilitate further understanding of fundamental principles to improve the device's performances and open up a new era for electrocatalysts and supercapacitors.

ACKNOWLEDGMENTS

This research was supported by the grants from the Research Grants Council of Hong Kong (CRF No. C7036-17W and GRF No. PolyU 153023/18P and PolyU Grant (1-ZVGH)).

REFERENCES

[1]F. Bonaccorso, L. Colombo, G. Yu, M. Stoller, V. Tozzini, A. C. Ferrari, R. S. Ruoff, and V. Pellegrini, Science **347**, 1246501 (2015).
[2]P. Zhang, F. Wang, M. Yu, X. Zhuang, and X. Feng, Chem. Soc. Rev. **47**, 7426–7451 (2018).
[3]Z. L. Wang, Nano Energy **68**, 104272 (2020).
[4]L. Huang, G. Bai, M. Wong, Z. Yang, W. Xu, and J. Hao, Adv. Mater. **28**, 2744–2751 (2016).
[5]W. Xu, L. Huang, M. Wong, L. Chen, G. Bai, and J. Hao, Adv. Energy Mater. **7**, 1601529 (2017).
[6]M. Wong, W. Xu, and J. Hao, Adv. Funct. Mater. **29**, 1904090 (2019).
[7]X. Cao, C. Tan, X. Zhang, W. Zhao, and H. Zhang, Adv. Mater. **28**, 6167–6196 (2016).
[8]Y. Da, J. Liu, L. Zhou, X. Zhu, X. Chen, and L. Fu, Adv. Mater **31**, 1802793 (2019).
[9]K. S. Kumar, N. Choudhary, Y. Jung, and J. Thomas, ACS Energy Lett. **3**, 482–495 (2018).
[10]M. Chhowalla, D. Voiry, J. Yang, H. S. Shin, and K. P. Loh, MRS Bull. **40**, 585–591 (2015).
[11]C. L. Tan, Z. C. Lai, and H. Zhang, Adv. Mater. **29**, 1701392 (2017).
[12]C. L. Tan and H. Zhang, Chem. Soc. Rev. **44**, 2713–2731 (2015).
[13]Y. Shi, H. Li, and L.-J. Li, Chem. Soc. Rev. **44**, 2744–2756 (2015).
[14]X. Zhang, Z. Lai, Q. Ma, and H. Zhang, Chem. Soc. Rev. **47**, 3301–3338 (2018).
[15]M. F. El-Kady, Y. Shao, and R. B. Kaner, Nat. Rev. Mater. **1**, 16033 (2016).
[16]J. R. Miller, R. A. Outlaw, and B. C. Holloway, Science **329**, 1637–1639 (2010).
[17]X. Yang, C. Cheng, Y. Wang, L. Qiu, and D. Li, Science **341**, 534–537 (2013).
[18]M. F. El-Kady, V. Strong, S. Dubin, and R. B. Kaner, Science **335**, 1326–1330 (2012).
[19]J. Xia, F. Chen, J. Li, and N. Tao, Nat. Nanotechnol. **4**, 505–509 (2009).
[20]J. Zhu, C. Yang, C. Lu, F. Zhang, Z. Yuan, and X. Zhuang, Acc. Chem. Res. **51**, 3191–3202 (2018).
[21]X. Zhuang, D. Gehrig, N. Forler, H. Liang, M. Wagner, M. R. Hansen, F. Laquai, F. Zhang, and X. Feng, Adv. Mater. **27**, 3789–3796 (2015).
[22]C. Wang, Q. He, U. Halim, Y. Liu, E. Zhu, Z. Lin, H. Xiao, X. Duan, Z. Feng, R. Cheng, N. O. Weiss, G. Ye, Y. Huang, H. Wu, H. Cheng, I. Shakir, L. Liao, X. Chen, W. A. Goddard III, Y. Huang, and X. Duan, Nature **555**, 231–236 (2018).
[23]Y. Liu, J. Guo, E. Zhu, L. Liao, S. Lee, M. Ding, I. Shakir, V. Gambin, Y. Huang, and X. Duan, Nature **557**, 696–700 (2018).
[24]J. Zhou, J. Lin, X. Huang, Y. Zhou, Y. Chen, J. Xia, H. Wang, Y. Xie, H. Yu, J. Lei, D. Wu, F. Liu, Q. Fu, Q. Zeng, C. Hsu, C. Yang, L. Lu, T. Yu, Z. Shen, H. Lin, B. I. Yakobson, Q. Liu, K. Suenaga, G. Liu, and Z. Liu, Nature **556**, 355–359 (2018).
[25]V. K. Sangwan, H. Lee, H. Bergeron, I. Balla, M. E. Beck, K. Chen, and M. C. Hersam, Nature **554**, 500–504 (2018).
[26]G. Bai, S. Yuan, Y. Zhao, Z. Yang, S. Y. Choi, Y. Chai, S. F. Yu, S. P. Lau, and J. Hao, Adv. Mater. **28**, 7472–7477 (2016).
[27]S. Yuan, Z. Yang, C. Xie, F. Yan, J. Dai, S. P. Lau, H. L. W. Chan, and J. Hao, Adv. Mater. **28**, 10048–10054 (2016).
[28]Z. Yang, J. Hao, S. Yuan, S. Lin, H. M. Yau, J. Dai, and S. P. Lau, Adv. Mater. **27**, 3748–3754 (2015).
[29]S. Yuan, X. Luo, H. L. Chan, C. Xiao, Y. Dai, M. Xie, and J. Hao, Nat. Commun. **10**, 1775 (2019).
[30]H. Chan, S. Yuan, and J. Hao, Phys. Status Solidi RRL **12**, 1800205 (2018).
[31]Y. Zhang, W. Jie, P. Chen, W. Liu, and J. Hao, Adv. Mater. **30**, 1707007 (2018).
[32]Y. Yang, H. Du, Q. Xue, X. Wei, Z. Yang, C. Xu, D. Lin, W. Jie, and J. Hao, Nano Energy **57**, 566 (2019).
[33]W. Io, S. Yuan, S. Pang, L. Wong, J. Zhao, and J. Hao, "Temperature- and thickness-dependence of robust out-of-plane ferroelectricity in CVD grown ultrathin van der Waals α-In_2Se_3 layers," Nano Res. (published online, 2020).
[34]Z. Yang, Z. Wu, Y. Lyu, and J. Hao, InfoMat **1**, 98 (2019).
[35]H. Du, J. Chen, M. Tu, S. Luo, S. Li, S. Yuan, T. Gong, W. Huang, W. Jie, and J. Hao, J. Mater. Chem. C **7**, 12160–12169 (2019).
[36]C. Tan, X. Cao, X. Wu, Q. He, J. Yang, X. Zhang, J. Chen, W. Zhao, S. Han, and G. Nam, Chem. Rev. **117**, 6225 (2017).
[37]Y. Zhong, X. Xia, F. Shi, J. Zhan, J. Tu, and H. J. Fan, Adv. Sci. **3**, 1500286 (2016).
[38]M. R. Lukatskaya, O. Mashtalir, C. E. Ren, Y. Dall'Agnese, P. Rozier, P. L. Taberna, M. Naguib, P. Simon, M. W. Barsoum, and Y. Gogotsi, Science **341**, 1502–1505 (2013).
[39]Y. Gogotsi and B. Anasori, ACS Nano **13**, 8491–8494 (2019).
[40]Z. Lei, W. Zhu, S. Xu, J. Ding, J. Wan, and P. Wu, ACS Appl. Mater. Interfaces **8**, 20900–20908 (2016).
[41]M. Chhowalla, H. S. Shin, G. Eda, L.-J. Li, K. P. Loh, and H. Zhang, Nat. Chem. **5**, 263–275 (2013).
[42]C. Zhan, M. Naguib, M. Lukatskaya, P. R. Kent, Y. Gogotsi, and D.-E. Jiang, J. Phys. Chem. Lett. **9**, 1223 (2018).
[43]D. Voiry, A. Mohite, and M. Chhowalla, Chem. Soc. Rev. **44**, 2702–2712 (2015).
[44]N. Uddin, H. Zhang, Y. Du, G. Jia, S. Wang, and Z. Yin, Adv. Mater. **32**, 1905739 (2020).
[45]B. Anasori, M. R. Lukatskaya, and Y. Gogotsi, Nat. Rev. Mater. **2**, 16098 (2017).
[46]A. Ambrosi, Z. Sofer, and M. Pumera, Chem. Commun. **51**, 8450–8453 (2015).
[47]D. Kong, H. Wang, J. J. Cha, M. Pasta, K. J. Koski, J. Yao, and Y. Cui, Nano Lett. **13**, 1341–1347 (2013).
[48]A. N. Enyashin, L. Yadgarov, L. Houben, I. Popov, M. Weidenbach, R. Tenne, M. Bar-Sadan, and G. Seifert, J. Phys. Chem. C **115**, 24586–24591 (2011).
[49]K. Qi, X. Cui, L. Gu, S. Yu, X. Fan, M. Luo, S. Xu, N. Li, L. Zheng, Q. Zhang, J. Ma, Y. Gong, F. Lv, K. Wang, H. Huang, W. Zhang, S. Guo, W. Zheng, and P. Liu, Nat. Commun. **10**, 5231 (2019).
[50]K. Chang, X. Hai, H. Pang, H. Zhang, L. Shi, G. Liu, H. Liu, G. Zhao, M. Li, and J. Ye, Adv. Mater. **28**, 10033–10041 (2016).
[51]H. Wang, C. Tsai, D. Kong, K. Chan, F. Abild-Pedersen, J. K. Nørskov, and Y. Cui, Nano Res. **8**, 566–575 (2015).
[52]M. Naguib, M. Kurtoglu, V. Presser, J. Lu, J. Niu, M. Heon, L. Hultman, Y. Gogotsi, and M. W. Barsoum, Adv. Mater. **23**, 4248–4253 (2011).
[53]S. F. Matar, Y. L. Petitcorps, and J. Etourneau, J. Mater. Chem. **7**, 99–103 (1997).
[54]M. Magnuson, O. Wilhelmsson, J.-P. Palmquist, U. Jansson, M. Mattesini, S. Li, R. Ahuja, and O. Eriksson, Phys. Rev. B **74**, 195108 (2006).
[55]M. Magnuson, M. Mattesini, O. Wilhelmsson, J. Emmerlich, J.-P. Palmquist, S. Li, R. Ahuja, L. Hultman, O. Eriksson, and U. Jansson, Phys. Rev. B **74**, 205102 (2006).
[56]O. Wilhelmsson, J.-P. Palmquist, E. Lewin, J. Emmerlich, P. Eklund, P. Å. Persson, H. Högberg, S. Li, R. Ahuja, and O. Eriksson, J. Cryst. Growth **291**, 290 (2006).
[57]T. Scabarozi, S. Amini, O. Leaffer, A. Ganguly, S. Gupta, W. Tambussi, S. Clipper, l. J. Spanier, M. Barsoum, and J. Hettinger, J. Appl. Phys. **105**, 013543 (2009).
[58]T. Li, L. Yao, Q. Liu, J. Gu, R. Luo, J. Li, X. Yan, W. Wang, P. Liu, B. Chen, W. Zhang, W. Abbas, R. Naz, and D. Zhang, Angew. Chem., Int. Ed. **57**, 6115–6119 (2018).
[59]X. Zhang, L. Hou, A. Ciesielski, and P. Samorì, Adv. Energy Mater. **6**, 1600671 (2016).
[60]C. Liu, X. Yan, F. Hu, G. Gao, G. Wu, and X. Yang, Adv. Mater. **30**, 1705713 (2018).
[61]Y. Jiao, A. M. Hafez, D. Cao, A. Mukhopadhyay, Y. Ma, and H. Zhu, Small **14**, 1800640 (2018).
[62]G. H. Han, D. L. Duong, D. H. Keum, S. J. Yun, and Y. H. Lee, Chem. Rev. **118**, 6297–6336 (2018).
[63]H. Yang, S. Kim, M. Chhowalla, and Y. H. Lee, Nat. Phys. **13**, 931–937 (2017).
[64]J. M. Soon and K. P. Loh, Solid-State Lett. **10**, A250–A254 (2007).
[65]Y. Liu, W. Wang, H. Huang, L. Gu, Y. Wang, and X. Peng, Chem. Commun. **50**, 4485–4488 (2014).
[66]S. K. Balasingam, J. S. Lee, and Y. Jun, Dalton Trans. **44**, 15491–15498 (2015).
[67]M. Acerce, D. Voiry, and M. Chhowalla, Nat. Nanotechnol. **10**, 313–318 (2015).
[68]X. Geng, Y. Zhang, Y. Han, J. Li, L. Yang, M. Benamara, L. Chen, and H. Zhu, Nano Lett. **17**, 1825–1832 (2017).

[69]X. Geng, W. Sun, W. Wu, B. Chen, A. Al-Hilo, M. Benamara, H. Zhu, F. Watanabe, J. Cui, and T. P. Chen, Nat. Commun. **7**, 10672 (2016).
[70]A. Khalil, Q. Liu, Q. He, T. Xiang, D. Liu, C. Wang, Q. Fang, and L. Song, RSC Adv. **6**, 48788–48791 (2016).
[71]P. Yu, W. Fu, Q. Zeng, J. Lin, C. Yan, Z. Lai, B. Tang, K. Suenaga, H. Zhang, and Z. Liu, Adv. Mater. **29**, 1701909 (2017).
[72]J. Wu, J. Peng, Z. Yu, Y. Zhou, Y. Guo, Z. Li, Y. Lin, K. Ruan, C. Wu, and Y. Xie, J. Am. Chem. Soc. **140**, 493–498 (2018).
[73]M. Liu, Z. Wang, J. Liu, G. Wei, J. Du, Y. Li, C. An, and J. Zhang, J. Mater. Chem. A **5**, 1035–1042 (2017).
[74]J. Feng, X. Sun, C. Wu, L. Peng, C. Lin, S. Hu, J. Yang, and Y. Xie, J. Am. Chem. Soc. **133**, 17832–17838 (2011).
[75]Q. Ji, C. Li, J. Wang, J. Niu, Y. Gong, Z. Zhang, Q. Fang, Y. Zhang, J. Shi, L. Liao, X. Wu, L. Gu, Z. Liu, and Y. Zhang, Nano Lett. **17**, 4908–4916 (2017).
[76]G. A. Muller, J. B. Cook, H. S. Kim, S. H. Tolbert, and B. Dunn, Nano Lett. **15**, 1911–1917 (2015).
[77]C. Wang, X. Wu, Y. Ma, G. Mu, Y. Li, C. Luo, H. Xu, Y. Zhang, J. Yang, X. Tang, J. Zhang, W. Bao, and C. Duan, J. Mater. Chem. A **6**, 8299–8306 (2018).
[78]X. Yu, S. Yun, J. S. Yeon, P. Bhattacharya, L. Wang, S. W. Lee, X. Hu, and H. S. Park, Adv. Energy Mater. **8**, 1702930 (2018).
[79]M. Liu, Y. Xu, Y. Hu, Q. Yang, L. Kong, W. Liu, W. Niu, and Y. Chueh, ACS Appl. Mater. Interfaces **10**, 35571–35579 (2018).
[80]X. Zang, C. Shen, E. Kao, R. Warren, R. Zhang, K. S. Teh, J. Zhong, M. Wei, B. Li, Y. Chu, M. Sanghadasa, A. Schwartzberg, and L. Lin, Adv. Mater. **30**, 1704754 (2018).
[81]B. Pandit, S. S. Karade, and B. R. Sankapal, ACS Appl. Mater. Interfaces **9**, 44880–44891 (2017).
[82]J. X. Zhu, W. P. Sun, D. Yang, Y. Zhang, H. H. Hoon, H. Zhang, and Q. Y. Yan, Small **11**, 4123–4129 (2015).
[83]J. Yang, C. Wang, H. Ju, Y. Sun, S. Xing, J. Zhu, and Q. Yang, Adv. Funct. Mater. **27**, 1703864 (2017).
[84]Q. Yun, Q. Lu, X. Zhang, C. Tan, and H. Zhang, Angew. Chem., Int. Ed. **57**, 626–646 (2018).
[85]K. Wang, J. Yang, J. Zhu, L. Li, Y. Liu, C. Zhang, and T. Liu, J. Mater. Chem. A **5**, 11236–11245 (2017).
[86]N. Choudhary, C. Li, H. Chung, J. Moore, J. Thomas, and Y. Jung, ACS Nano **10**, 10726–10735 (2016).
[87]J. Tian, H. Zhang, and Z. Li, ACS Appl. Mater. Interfaces **10**, 29511–29520 (2018).
[88]S. Peng, L. Li, H. Tan, R. Cai, W. Shi, C. Li, S. G. Mhaisalkar, M. Srinivasan, S. Ramakrishna, and Q. Yan, Adv. Funct. Mater. **24**, 2155–2162 (2014).
[89]N. Parveen, S. A. Ansari, H. R. Alamri, M. O. Ansari, Z. Khan, and M. H. Cho, ACS Omega **3**, 1581–1588 (2018).
[90]S. Pang, Y. Wong, S. Yuan, Y. Liu, M. Tsang, Z. Yang, H. Huang, W. Wong, and J. Hao, J. Am. Chem. Soc. **141**, 9610–9616 (2019).
[91]A. Lipatov, M. Alhabeb, M. R. Lukatskaya, A. Boson, Y. Gogotsi, and A. Sinitskii, Adv. Electron. Mater. **2**, 1600255 (2016).
[92]V. Augustyn, P. Simon, and B. Dunn, Energy Environ. Sci. **7**, 1597–1614 (2014).
[93]C. Hao, B. Yang, F. Wen, J. Xiang, L. Li, W. Wang, Z. Zeng, B. Xu, Z. Zhao, and Z. Liu, Adv. Mater. **28**, 3194–3201 (2016).
[94]H. Xiao, Z.-S. Wu, L. Chen, F. Zhou, S. Zheng, W. Ren, H.-M. Cheng, and X. Bao, ACS Nano **11**, 7284–7292 (2017).
[95]C. X. Guo and C. M. Li, Energy Environ. Sci. **4**, 4504–4507 (2011).
[96]J. Pang, A. Bachmatiuk, Y. Yin, B. Trzebicka, L. Zhao, L. Fu, R. G. Mendes, T. Gemming, Z. Liu, and M. H. Rummeli, Adv. Energy Mater. **8**, 1702093 (2018).
[97]A. D. Handoko, K. D. Fredrickson, B. Anasori, K. W. Convey, L. R. Johnson, Y. Gogotsi, A. Vojvodic, and Z. W. Seh, ACS Appl. Energy Mater. **1**, 173–180 (2018).
[98]S. Li, P. Tuo, J. Xie, X. Zhang, J. Xu, J. Bao, B. Pan, and Y. Xie, Nano Energy **47**, 512–518 (2018).
[99]M. R. Lukatskaya, J. Halim, B. Dyatkin, M. Naguib, Y. S. Buranova, M. W. Barsoum, and Y. Gogotsi, Angew. Chem., Int. Ed. **53**, 4877–4880 (2014).
[100]Z. W. Seh, K. D. Fredrickson, B. Anasori, J. Kibsgaard, A. L. Strickler, M. R. Lukatskaya, Y. Gogotsi, T. F. Jaramillo, and A. Vojvodic, ACS Energy Lett. **1**, 589–594 (2016).
[101]A. VahidMohammadi, A. Hadjikhani, S. Shahbazmohamadi, and M. Beidaghi, ACS Nano **11**, 11135–11144 (2017).
[102]M. Hu, T. Hu, Z. Li, Y. Yang, R. Cheng, J. Yang, C. Cui, and X. Wang, ACS Nano **12**, 3578–3586 (2018).
[103]S. Kajiyama, L. Szabova, H. Iinuma, A. Sugahara, K. Gotoh, K. Sodeyama, Y. Tateyama, M. Okubo, and A. Yamada, Adv. Energy Mater. **7**, 1601873 (2017).
[104]M. Hu, Z. Li, H. Zhang, T. Hu, C. Zhang, Z. Wu, and X. Wang, Chem. Commun. **51**, 13531–13533 (2015).
[105]J. Luo, X. Tao, J. Zhang, Y. Xia, H. Huang, L. Zhang, Y. Gan, C. Liang, and W. Zhang, ACS Nano **10**, 2491–2499 (2016).
[106]S. Lai, J. Jeon, S. K. Jang, J. Xu, Y. J. Choi, J.-H. Park, E. Hwang, and S. Lee, Nanoscale **7**, 19390–19396 (2015).
[107]M. Naguib and Y. Gogotsi, Acc. Chem. Res. **48**, 128–135 (2015).
[108]O. Mashtalir, M. Naguib, V. N. Mochalin, Y. Dall'Agnese, M. Heon, M. W. Barsoum, and Y. Gogotsi, Nat. Commun. **4**, 1716 (2013).
[109]T. Y. Ma, J. L. Cao, M. Jaroniec, and S. Z. Qiao, Angew. Chem., Int. Ed. **55**, 1138–1142 (2016).
[110]M. Ghidiu, M. R. Lukatskaya, M.-Q. Zhao, Y. Gogotsi, and M. W. Barsoum, Nature **516**, 78–81 (2014).
[111]L. G. Sillen, A. E. Martell, and J. Bjerrum, J. Chem. Educ. **42**, 521 (1965).
[112]X. Xie, Y. Xue, L. Li, S. Chen, Y. Nie, W. Ding, and Z. Wei, Nanoscale **6**, 11035–11040 (2014).
[113]J. Xuan, Z. Wang, Y. Chen, D. Liang, L. Cheng, X. Yang, Z. Liu, R. Ma, T. Sasaki, and F. Geng, Angew. Chem., Int. Ed. **128**, 14789–14794 (2016).
[114]G. Zou, J. Guo, X. Liu, Q. Zhang, G. Huang, C. Fernandez, and Q. Peng, Adv. Energy Mater. **7**, 1700700 (2017).
[115]G. Zou, Q. Zhang, C. Fernandez, G. Huang, J. Huang, and Q. Peng, ACS Nano **11**, 12219–12229 (2017).
[116]Y. Dall'Agnese, M. R. Lukatskaya, K. M. Cook, P.-L. Taberna, Y. Gogotsi, and P. Simon, Electrochem. Commun. **48**, 118–122 (2014).
[117]M. R. Lukatskaya, S. Kota, Z. Lin, M.-Q. Zhao, N. Shpigel, M. D. Levi, J. Halim, P.-L. Taberna, M. W. Barsoum, and P. Simon, Nat. Energy **2**, 17105 (2017).
[118]S. Yang, P. Zhang, F. Wang, A. G. Ricciardulli, M. R. Lohe, P. W. Blom, and X. Feng, Angew. Chem. **130**, 15717 (2018).
[119]J. Li, X. Yuan, C. Lin, Y. Yang, L. Xu, X. Du, J. Xie, J. Lin, and J. Sun, Adv. Energy Mater. **7**, 1602725 (2017).
[120]E. Kayali, A. VahidMohammadi, J. Orangi, and M. Beidaghi, ACS Appl. Mater. Interfaces **10**, 25949–25954 (2018).
[121]T.-H. Chang, T. Zhang, H. Yang, K. Li, Y. Tian, J. Y. Lee, and P.-Y. Chen, ACS Nano **12**, 8048–8059 (2018).
[122]J. Zhang, S. Seyedin, S. Qin, Z. Wang, S. Moradi, F. Yang, P. A. Lynch, W. Yang, J. Liu, and X. Wang, Small **15**, 1804732 (2019).
[123]A. S. Levitt, M. Alhabeb, C. B. Hatter, A. Sarycheva, G. Dion, and Y. Gogotsi, J. Mater. Chem. A **7**, 269 (2019).
[124]W. Tian, A. VahidMohammadi, M. S. Reid, Z. Wang, L. Ouyang, J. Erlandsson, T. Pettersson, L. Wågberg, M. Beidaghi, and M. M. Hamedi, Adv. Mater. **31**, 1902977 (2019).
[125]Y. Yoon, M. Lee, S. K. Kim, G. Bae, W. Song, S. Myung, J. Lim, S. S. Lee, T. Zyung, and K. S. An, Adv. Energy Mater. **8**, 1703173 (2018).
[126]Z. Pan and X. Ji, J. Power Sources **439**, 227068 (2019).
[127]H. Li, X. Li, J. Liang, and Y. Chen, Adv. Energy Mater. **9**, 1803987 (2019).
[128]M. Hu, C. Cui, C. Shi, Z.-S. Wu, J. Yang, R. Cheng, T. Guang, H. Wang, H. Lu, and X. Wang, ACS Nano **13**, 6899 (2019).
[129]W. Zhao, J. Peng, W. Wang, B. Jin, T. Chen, S. Liu, Q. Zhao, and W. Huang, Small **15**, 1901351 (2019).
[130]L. Yu, L. Hu, B. Anasori, Y. T. Liu, Q. Zhu, P. Zhang, Y. Gogotsi, and B. Xu, ACS Energy Lett. **3**, 1597–1603 (2018).
[131]H. Li, Y. Hou, F. Wang, M. R. Lohe, X. Zhuang, L. Niu, and X. Feng, Adv. Energy Mater. **7**, 1601847 (2017).
[132]X. Chen, S. Wang, J. Shi, X. Du, Q. Cheng, R. Xue, Q. Wang, M. Wang, L. Ruan, and W. Zeng, Adv. Mater. Interfaces **6**, 1901160 (2019).
[133]X. Wang, H. Li, H. Li, S. Lin, W. Ding, X. Zhu, Z. Sheng, H. Wang, X. Zhu, and Y. Sun, Adv. Funct. Mater. **30**, 0190302 (2020).
[134]Y. Zhou, K. Maleski, B. Anasori, J. O. Thostenson, Y. Pang, Y. Feng, K. Zeng, C. B. Parker, S. Zauscher, Y. Gogotsi, J. T. Glass, and C. Cao, ACS Nano **14**, 3576 (2020).

[135]C. Wu, B. Unnikrishnan, I. P. Chen, S. G. Harroun, H. Chang, and C. Huang, Energy Storage Mater. **25**, 563–571 (2020).
[136]K. Li, X. Wang, S. Li, P. Urbankowski, J. Li, Y. Xu, and Y. Gogotsi, Small **16**, 1906851 (2020).
[137]X. Li, H. Wu, C. Guan, A. M. Elshahawy, Y. Dong, S. J. Pennycook, and J. Wang, Small **15**, 1803895 (2018).
[138]J. Yuan, D. Yao, L. Jiang, Y. Tao, J. Che, G. He, and H. Chen, ACS Appl. Mater. Interfaces **3**, 1794–1803 (2020).
[139]S. Saha, M. Jana, P. Khanra, P. Samanta, H. Koo, N. C. Murmu, and T. Kuila, ACS Appl. Mater. Interfaces **7**, 14211–14222 (2015).
[140]L. B. Huang, W. Xu, and J. Hao, Small **13**, 1701820 (2017).
[141]Z. L. Wang and A. C. Wang, Mater. Today **30**, 34–51 (2019).
[142]L. B. Huang, W. Xu, G. Bai, M.-C. Wong, Z. Yang, and J. Hao, Nano Energy **30**, 36 (2016).
[143]W. Xu, M.-C. Wong, and J. Hao, Nano Energy **55**, 203 (2019).
[144]J. A. Turner, Science **305**, 972 (2004).
[145]B. Conway and L. Bai, Electrochim. Acta **31**, 1013 (1986).
[146]M. Dresselhaus and I. Thomas, Nature **414**, 332 (2001).
[147]B. Conway and L. Bai, J. Electroanal. Chem. **198**, 149 (1986).
[148]D. Deng, K. S. Novoselov, Q. Fu, N. Zheng, Z. Tian, and X. Bao, Nat. Nanotechnol. **11**, 218–230 (2016).
[149]J. Di, C. Yan, A. D. Handoko, Z. W. Seh, H. Li, and Z. Liu, Mater. Today **21**, 749–770 (2018).
[150]H. Jin, C. Guo, X. Liu, J. Liu, A. Vasileff, Y. Jiao, Y. Zheng, and S. Qiao, Chem. Rev. **118**, 6337–6408 (2018).
[151]D. Voiry, R. Fullon, J. Yang, E. S. C. de Carvalho Castro, R. Kappera, I. Bozkurt, D. Kaplan, M. J. Lagos, P. E. Batson, G. Gupta, A. D. Mohite, L. Dong, D. Er, V. B. Shenoy, T. Asefa, and M. Chhowalla, Nat. Mater. **15**, 1003–1009 (2016).
[152]H. Li, C. Tsai, A. L. Koh, L. Cai, A. W. Contryman, A. H. Fragapane, J. Zhao, H. S. Han, H. C. Manoharan, F. Abild-Pedersen, J. K. Nørskov, and X. Zheng, Nat. Mater. **15**, 48–53 (2016).
[153]Q. Ding, B. Song, P. Xu, and S. Jin, Chem **1**, 699–726 (2016).
[154]Y. Qu, H. Medina, S. Wang, Y. Wang, C. Chen, T. Su, A. Manikandan, K. Wang, Y. Shih, J. Chang, H. Kuo, C. Lee, S. Lu, G. Shen, Z. M. Wang, and Y. Chueh, Adv. Mater. **28**, 9831–9838 (2016).
[155]D. Er, H. Ye, N. C. Frey, H. Kumar, J. Lou, and V. B. Shenoy, Nano Lett **18**, 3943–3949 (2018).
[156]Z. Lei, J. Zhan, L. Tang, Y. Zhang, and Y. Wang, Adv. Energy Mater. **8**, 1703482 (2018).
[157]G. Zhao, K. Rui, S. X. Dou, and W. Sun, Adv. Funct. Mater. **28**, 1803291 (2018).
[158]Y. Zhu, L. Peng, Z. Fang, C. Yan, X. Zhang, and G. Yu, Adv. Mater. **30**, 1706347 (2018).
[159]B. Hinnemann, P. G. Moses, J. Bonde, K. P. Jørgensen, J. H. Nielsen, S. Horch, I. Chorkendorff, and J. K. Nørskov, J. Am. Chem. Soc. **127**, 5308–5309 (2005).
[160]T. F. Jaramillo, K. P. Jørgensen, J. Bonde, J. H. Nielsen, S. Horch, and I. Chorkendorff, Science **317**, 100–102 (2007).
[161]D. Voiry, J. Yang, and M. Chhowalla, Adv. Mater. **28**, 6197–6206 (2016).
[162]J. Xie, H. Zhang, S. Li, R. Wang, X. Sun, M. Zhou, J. Zhou, X. W. Lou, and Y. Xie, Adv. Mater. **25**, 5807–5813 (2013).
[163]G. Ye, Y. Gong, J. Lin, B. Li, Y. He, S. T. Pantelides, W. Zhou, R. Vajtai, and P. M. Ajayan, Nano Lett. **16**, 1097–1103 (2016).
[164]Y. Guo, X. Zhang, X. Zhang, and T. You, J. Mater. Chem. A **3**, 15927–15934 (2015).
[165]Y. Zheng, P. Wu, M. Gao, X. Zhang, F. Gao, H. Ju, R. Wu, Q. Gao, R. You, W. Huang, S. Liu, S. Hu, J. Zhu, Z. Li, and S. Yu, Nat. Commun. **9**, 2533 (2018).
[166]C. Jian, Q. Cai, W. Hong, J. Li, and W. Liu, Small **14**, 1703798 (2018).
[167]S. Liu, M. Li, C. Wang, P. Jiang, L. Hu, and Q. Chen, ACS Sustainable Chem. Eng. **6**, 9137–9144 (2018).
[168]M. A. Lukowski, A. S. Daniel, F. Meng, A. Forticaux, L. Li, and S. Jin, J. Am. Chem. Soc. **135**, 10274–10277 (2013).
[169]Y. Yu, G. Nam, Q. He, X. Wu, K. Zhang, Z. Yang, J. Chen, Q. Ma, M. Zhao, Z. Liu, F. Ran, X. Wang, H. Li, X. Huang, B. Li, Q. Xiong, Q. Zhang, Z. Liu, L. Gu, Y. Du, W. Huang, and H. Zhang, Nat. Chem. **10**, 638–643 (2018).
[170]Y. Zhou, E. Song, J. Zhou, J. Lin, R. Ma, Y. Wang, W. Qiu, R. Shen, K. Suenaga, Q. Liu, J. Wang, Z. Liu, and J. Liu, ACS Nano **12**, 4486–4493 (2018).
[171]C. Tan, Z. Luo, A. Chaturvedi, Y. Cai, Y. Du, Y. Gong, Y. Huang, Z. Lai, X. Zhang, L. Zheng, X. Qi, M. H. Goh, J. Wang, S. Han, X. Wu, L. Gu, C. Kloc, and H. Zhang, Adv. Mater. **30**, 1705509 (2018).
[172]Z. Lai, A. Chaturvedi, Y. Wang, T. H. Tran, X. Liu, C. Tan, Z. Luo, B. Chen, Y. Huang, G. Nam, Z. Zhang, Y. Chen, Z. Hu, B. Li, S. Xi, Q. Zhang, Y. Zong, L. Gu, C. Kloc, Y. Du, and H. Zhang, J. Am. Chem. Soc. **140**, 8563–8568 (2018).
[173]S. M. Tan, Z. Sofer, J. Luxa, and M. Pumera, ACS Catal. **6**, 4594–4607 (2016).
[174]Y. Yin, Y. Zhang, T. Gao, T. Yao, X. Zhang, J. Han, X. Wang, Z. Zhang, P. Xu, P. Zhang, X. Cao, B. Song, and S. Jin, Adv. Mater. **29**, 1700311 (2017).
[175]M. Jiang, J. Zhang, M. Wu, W. Jian, H. Xue, T. Ng, C. Lee, and J. Xu, J. Mater. Chem. A **4**, 14949–14953 (2016).
[176]L. Najafi, S. Bellani, R. Oropesa-Nuñez, A. Ansaldo, M. Prato, A. E. D. R. Castillo, and F. Bonaccorso, Adv. Energy Mater. **8**, 1703212 (2018).
[177]L. Najafi, S. Bellani, R. Oropesa-Nuñez, A. Ansaldo, M. Prato, A. E. D. R. Castillo, and F. Bonaccorso, Adv. Energy Mater. **8**, 1801764 (2018).
[178]Q. F. Gong, L. Cheng, C. Liu, M. Zhang, Q. Feng, H. Ye, M. Zeng, L. Xie, Z. Liu, and Y. Li, ACS Catal. **5**, 2213–2219 (2015).
[179]D. Voiry, H. Yamaguchi, J. Li, R. Silva, D. C. Alves, T. Fujita, M. Chen, T. Asefa, V. B. Shenoy, G. Eda, and M. Chhowalla, Nat. Mater. **12**, 850–855 (2013).
[180]M. A. Lukowski, A. S. Daniel, C. R. English, F. Meng, A. Forticaux, R. J. Hamers, and S. Jin, Energy Environ. Sci. **7**, 2608–2613 (2014).
[181]J. Zhang, C. Zhang, Z. Wang, J. Zhu, Z. Wen, X. Zhao, X. Zhang, J. Xu, and Z. Lu, Small **14**, 1703098 (2018).
[182]M. Yan, X. Pan, P. Wang, F. Chen, L. He, G. Jiang, J. Wang, J. Z. Liu, X. Xu, X. Liao, J. Yang, and L. Mai, Nano Lett. **17**, 4109–4115 (2017).
[183]J. Zhang, W. Xiao, P. Xi, S. Xi, Y. Du, D. Gao, and J. Ding, ACS Energy Lett. **2**, 1022–1028 (2017).
[184]J. Li, M. Hong, L. Sun, W. Zhang, H. Shu, and H. Chang, ACS Appl. Mater. Interfaces **10**, 458–467 (2018).
[185]Y. Feng, S. Gong, E. Du, X. Chen, R. Qi, K. Yu, and Z. Zhu, J. Phys. Chem. C **122**, 2382–2390 (2018).
[186]X. Chia, Z. Sofer, J. Luxa, and M. Pumera, ACS Appl. Mater. Interfaces **9**, 25587–25599 (2017).
[187]X. Chia and M. Pumera, Nat. Catal. **1**, 909–921 (2018).
[188]J. Zhang, Y. Zhao, X. Guo, C. Chen, C. Dong, R. Liu, C. Han, Y. Li, Y. Gogotsi, and G. Wang, Nat. Catal. **1**, 985–992 (2018).
[189]M. Pandey and K. S. Thygesen, J. Phys. Chem. C **121**, 13593–13598 (2017).
[190]H. Pan, Sci. Rep. **6**, 32531 (2016).
[191]C. Ling, L. Shi, Y. Ouyang, Q. Chen, and J. Wang, Adv. Sci. **3**, 1600180 (2016).
[192]S. Zhou, X. Yang, W. Pei, N. Liu, and J. Zhao, Nanoscale **10**, 10876–10883 (2018).
[193]G. Gao, A. P. O'Mullane, and A. Du, ACS Catal. **7**, 494–500 (2017).
[194]B. Anasori, C. Shi, E. J. Moon, Y. Xie, C. A. Voigt, P. R. Kent, S. J. May, S. J. Billinge, M. W. Barsoum, and Y. Gogotsi, Nanoscale Horiz. **1**, 227–234 (2016).
[195]M. Q. Zhao, X. Xie, C. E. Ren, T. Makaryan, B. Anasori, G. Wang, and Y. Gogotsi, Adv. Mater. **29**, 1702410 (2017).
[196]L. Xiu, Z. Wang, M. Yu, X. Wu, and J. Qiu, ACS Nano **12**, 8017–8028 (2018).
[197]M. Yu, Z. Wang, J. Liu, F. Sun, P. Yang, and J. Qiu, Nano Energy **63**, 103880 (2019).
[198]W. Yuan, L. Cheng, Y. An, H. Wu, N. Yao, X. Fan, and X. Guo, ACS Sustainable Chem. Eng. **6**, 8976 (2018).
[199]Z. Li, Z. Qi, S. Wang, T. Ma, L. Zhou, Z. Wu, X. Luan, F.-Y. Lin, M. Chen, and J. T. Miller, Nano Lett. **19**, 5102 (2019).
[200]Y. Jiang, X. Wu, Y. Yan, S. Luo, X. Li, J. Huang, H. Zhang, and D. Yang, Small **15**, 1805474 (2019).
[201]Y. Yuan, H. Li, L. Wang, L. Zhang, D. Shi, Y. Hong, and J. Sun, ACS Sustainable Chem. Eng. **7**, 4266 (2019).
[202]V. Ramalingam, P. Varadhan, H. C. Fu, H. Kim, D. Zhang, S. Chen, L. Song, D. Ma, Y. Wang, and H. N. Alshareef, Adv. Mater. **31**, 1903841 (2019).
[203]Y. Yoon, A. P. Tiwari, M. Choi, T. G. Novak, W. Song, H. Chang, T. Zyung, S. S. Lee, S. Jeon, and K. S. An, Adv. Funct. Mater. **29**, 1903443 (2019).
[204]J. You, C. Si, J. Zhou, and Z. Sun, J. Phys. Chem. C **123**, 3719 (2019).
[205]J. Liang, C. Ding, J. Liu, T. Chen, W. Peng, Y. Li, F. Zhang, and X. Fan, Nanoscale **11**, 10992 (2019).
[206]Y. Hou, M. Qiu, G. Nam, M. Kim, T. Zhang, K. Liu, X. Zhuang, J. Cho, C. Yuan, and X. Feng, Nano Lett. **17**, 4202–4209 (2017).

[207]L. He, J. Liu, Y. Liu, B. Cui, B. Hua, M. Wang, K. Tiana, Y. Song, S. Wu, Z. Zhan, Z. Peng, and M. Du, Appl. Catal. B **248**, 366–379 (2019).
[208]W. Li, D. Liu, N. Yang, J. Wang, M. Huanga, L. Liu, X. Peng, G. Wang, X. Yu, and P. K. Chu, Appl. Surf. Sci **467–468**, 328–334 (2019).
[209]L. Jiang, L. Qiu, T. Cen, Y. Liu, X. Peng, Z. Ye, and D. Yuan, Chem. Commun. **56**, 567–570 (2020).
[210]M. Shakeel, M. Arif, G. Yasin, B. Li, and H. D. Khan, Appl. Catal. B **242**, 485–498 (2019).
[211]L. Wang, Z. Sofer, and M. Pumera, ACS Nano **14**, 21–25 (2020).
[212]S. Pang, W. Io, L. Wong, J. Zhao, and J. Hao, "Efficient energy conversion and storage based on robust fluoride-free self-assembled 1D niobium carbide in 3D nanowire network," Adv. Sci. (published online, 2020).